

Transferrin receptor 1 ablation in satellite cells impedes skeletal muscle regeneration through activation of ferroptosis

Hongrong Ding^{1,2†}, Shujie Chen^{1,3†}, Xiaohan Pan^{1†}, Xiaoshuang Dai^{4†}, Guihua Pan¹, Ze Li^{1,3}, Xudong Mai^{1,3}, Ye Tian^{1,3}, Susu Zhang^{1,3}, Bingdong Liu¹, Guangchao Cao⁵, Zhicheng Yao⁶, Xiangping Yao^{1,3}, Liang Gao¹, Li Yang⁶, Xiaoyan Chen⁶, Jia Sun³, Hong Chen³, Mulan Han¹, Yulong Yin^{1,7}, Guohuan Xu¹, Huijun Li⁸, Weidong Wu⁸, Zheng Chen⁹, Jingchao Lin¹⁰, Liping Xiang¹¹, Jun Hu^{12*}, Yan Lu^{11*}, Xiao Zhu^{2*} & Liwei Xie^{1,3,8*} 

¹Guangdong Provincial Key Laboratory of Microbial Culture Collection and Application, State Key Laboratory of Applied Microbiology Southern China, Institute of Microbiology, Guangdong Academy of Sciences, Guangzhou, China; ²Guangdong Provincial Key Laboratory of Molecular Diagnosis, The Marine Biomedical Research Institute, Guangdong Medical University, Zhanjiang, China; ³Department of Endocrinology and Metabolism, Zhujiang Hospital, Southern Medical University, Guangzhou, China; ⁴BGI Institute of Applied Agriculture, BGI-Shenzhen, Shenzhen, China; ⁵The Biomedical Translational Research Institute, Faculty of Medical Science, Jinan University, Guangzhou, China; ⁶The Third Affiliated Hospital of Sun Yat-Sen University, Guangzhou, China; ⁷China Institute of Subtropical Agriculture, Chinese Academy of Sciences, Changsha, Hunan, China; ⁸College of Public Health, Xinxiang Medical University, Xinxiang, China; ⁹HIT Center for Life Sciences, School of Life Science and Technology, Harbin Institute of Technology, Harbin, China; ¹⁰Metabo-Profile Biotechnology (Shanghai) Co. Ltd., Shanghai, China; ¹¹Key Laboratory of Metabolism and Molecular Medicine, The Ministry of Education, Department of Endocrinology and Metabolism, Zhongshan Hospital, Fudan University, Shanghai, China; ¹²Department of Orthopedics, The First Affiliated Hospital of Nanjing Medical University, Nanjing, Jiangsu, China

Abstract

Background Satellite cells (SCs) are critical to skeletal muscle regeneration. Inactivation of SCs is linked to skeletal muscle loss. Transferrin receptor 1 (Tfr1) is associated with muscular dysfunction as muscle-specific deletion of *Tfr1* results in growth retardation, metabolic disorder, and lethality, shedding light on the importance of Tfr1 in muscle physiology. However, its physiological function regarding skeletal muscle ageing and regeneration remains unexplored.

Methods RNA sequencing is applied to skeletal muscles of different ages to identify Tfr1 associated to skeletal muscle ageing. Mice with conditional SC ablation of *Tfr1* were generated. Between *Tfr1*^{SC/WT} and *Tfr1*^{SC/KO} ($n = 6–8$ mice per group), cardiotoxin was intramuscularly injected, and transverse abdominal muscle was dissected, weighted, and cryosectioned, followed by immunostaining, haematoxylin and eosin staining, and Masson staining. These phenotypical analyses were followed with functional analysis such as flow cytometry, tread mill, Prussian blue staining, and transmission electron microscopy to identify pathological pathways that contribute to regeneration defects.

Results By comparing gene expression between young (2 weeks old, $n = 3$) and aged (80 weeks old, $n = 3$) mice among four types of muscles, we identified that *Tfr1* expression is declined in muscles of aged mice (~80% reduction, $P < 0.005$), so as to its protein level in SCs of aged mice. From *in vivo* and *ex vivo* experiments, *Tfr1* deletion in SCs results in an irreversible depletion of SCs (~60% reduction, $P < 0.005$) and cell-autonomous defect in SC proliferation and differentiation, leading to skeletal muscle regeneration impairment, followed by labile iron accumulation, lipogenesis, and decreased Gpx4 and Nrf2 protein levels leading to reactive oxygen species scavenger defects. These abnormal phenomena including iron accumulation, activation of unsaturated fatty acid biosynthesis, and lipid peroxidation are orchestrated with the occurrence of ferroptosis in skeletal muscle. Ferroptosis further exacerbates SC proliferation and skeletal muscle regeneration. Ferrostatin-1, a ferroptosis inhibitor, could not rescue ferroptosis. However, intramuscular administration of lentivirus-expressing Tfr1 could partially reduce labile iron accumulation, decrease lipogenesis, and promote skeletal muscle regeneration. Most importantly, declined Tfr1 but increased Slc39a14 protein level on cellular membrane contributes to labile iron accumulation in skeletal muscle of aged rodents (~80 weeks old), leading to activation of ferroptosis in aged skeletal muscle. This is inhibited by ferrostatin-1 to improve running time ($P = 0.0257$) and distance ($P = 0.0248$).

Conclusions Satellite cell-specific deletion of *Tfr1* impairs skeletal muscle regeneration with activation of ferroptosis. This phenomenon is recapitulated in skeletal muscle of aged rodents and human sarcopenia. Our study provides mechanistic information for developing novel therapeutic strategies against muscular ageing and diseases.

Keywords Tfr1; Satellite cells; Ferroptosis; Fibro/adipogenic progenitors

Received: 26 November 2020; Revised: 18 February 2021; Accepted: 16 March 2021

*Correspondence to: Jun Hu, Department of Orthopedics, The First Affiliated Hospital of Nanjing Medical University, Nanjing, Jiangsu, China. Email: junhu@njmu.edu.cn
Yan Lu, Key Laboratory of Metabolism and Molecular Medicine, The Ministry of Education, Department of Endocrinology and Metabolism, Zhongshan Hospital, Fudan University, Shanghai, China. Email: lu.yan2@zs-hospital.sh.cn

Xiao Zhu, Guangdong Provincial Key Laboratory of Molecular Diagnosis, The Marine Biomedical Research Institute, Guangdong Medical University, Zhanjiang, China. Email: biox Zhu@yahoo.com

Liwei Xie, Guangdong Provincial Key Laboratory of Microbial Culture Collection and Application, State Key Laboratory of Applied Microbiology Southern China, Institute of Microbiology, Guangdong Academy of Sciences, Guangzhou, China. Email: xielw@gdim.cn

†These authors contributed equally to this work.

Introduction

Programmed cell death, such as apoptosis, autophagy, and the newly discovered programmed necrosis (also named necroptosis), is a critical process to remove dead, non-essential, or senescent cells during organism and organ development/regeneration.¹ Skeletal muscle is a major organ not only supporting movement but also regulating systemic metabolism. Muscle cell death occurs in multiple forms, such as apoptosis, necrosis, and autophagy.² Under regenerative conditions, cell death, clearance, and regeneration are precisely regulated, while dysregulation of these processes leads to muscular dystrophy, sarcopenia, and pathogenesis.² Necrosis of skeletal muscle occurs under various pathogenic conditions, such as muscular dystrophy and ischaemia. However, acute or physiological injuries can activate apoptosis, which is regulated by several crucial molecules, such as an anti-apoptotic oncoproteins Bcl2, caspase 3, and the death receptor Fas/Apo1/Cd95.³ This process is accompanied by infiltration of inflammatory leucocytes, especially macrophages. At the initial stage of regeneration, M1 macrophages are indispensable for cytokine secretion, fibre debris clearance, and iron recycling as well as myoblasts, fibroadipogenic precursor cells (FAPs), and immune cells balancing during skeletal muscle regeneration.² Upon completion of fibre debris clearance, M1 macrophages are transformed into M2 macrophages contributing to secretion of anti-inflammatory cytokines and promoting regeneration.²

Along with these findings, ferroptosis, a newly identified distinct cell death pathway, is involved in development of a plethora of diseases, such as cancers, ischaemia/reperfusion-induced cardiomyopathy, degenerative diseases, and stroke. Ferroptosis is an iron-dependent and reactive oxygen species (ROS)-dependent oxidative damage via accumulation of lipid peroxides.⁴ Cells experiencing ferroptosis are characterized by a variety of cytological changes and abnormalities of the mitochondria, including decreased or vanished mitochondrial cristae, and a ruptured or condensed mitochondrial membrane.⁴ A recent study suggested that during the development of cardiomyopathy death, Nrf2-mediated

up-regulation of *Hmox1* contributes to free iron release from haem degradation, leading to lipid peroxidation on mitochondrial lipid bilayer as the major mechanism in ferroptosis-induced heart damage.⁵ Other diseases, such as liver fibrosis or cirrhosis, are also linked to iron-dependent cell death. Patients with liver cirrhosis are diagnosed with higher iron contents and lipid peroxidation but lower levels of transferrin (Trf).⁶ Liver-specific *Trf*-deletion mice are susceptible to the development of ferroptosis-induced liver fibrosis under a high-iron diet.⁶ Moreover, the pathogenic property of ferroptosis has not been reported in other organs, such as skeletal muscle.

Skeletal muscle growth and regeneration rely on a subtype of adult stem cells developed from mesodermal layer, namely, satellite cells (SCs).⁷ SCs are considered as adult stem cells because they maintain self-renewal and remarkable postnatal regenerative potential in skeletal muscle. Quiescent SCs are located between the basal lamina and plasma membrane of myofibres. They are activated by external stimulation or muscle injury, followed by entering the cell cycle, proliferation, and differentiation to repair injured myotubes.⁷ This process is regulated by a group of myogenic regulatory factors, including but not limited to MyoD and myogenin.⁷ Some other newly identified transcription factors are also involved in regulating SC physiology and are further extended to skeletal muscle development and regeneration, for example, Yin Yang 1 (YY1)⁸ and hypoxia-inducible factor 2 α (HIF2 α).⁹ The dysregulation results in dysfunction of SCs and eventually the growth and regeneration impairment.

Meanwhile, skeletal muscle growth and regeneration are accompanied by a precise regulation of various nutrients, such as amino acids, carbohydrates, and minerals. Trace minerals, as key nutritional components, play an important role in skeletal muscle physiology and energy metabolism. Iron, as an essential trace mineral, is required to maintain the appropriate function of skeletal muscles, such as muscle cell differentiation, skeletal muscle growth, and myoglobin biosynthesis. Iron is released from food and absorbed by epithelial cells of the small intestine. In the blood circulation, transferrin-bound iron (TBI) is recognized, internalized, and

absorbed by the action of transferrin receptor 1 (Tfr1), which is ubiquitously expressed in peripheral tissues such as liver, adipose tissue, and skeletal muscles. Thus, Tfr1-mediated iron homeostasis is a rate-limiting step in regulating tissue growth and regeneration. It has been demonstrated that skeletal muscle-specific knockout of *Tfr1* blocks iron absorption and leads to pathological and metabolic changes in skeletal muscle, liver, and adipose tissue.^{10,11} Other studies indicated that iron in skeletal muscle is locally recycled with the involvement of myoblasts and macrophages at different stages of regeneration.¹² Dysregulation of skeletal muscle iron metabolism, especially labile iron accumulation, may impair skeletal muscle regeneration.¹² However, the biological function of Tfr1 in SC physiology especially during skeletal muscle regeneration still remains unknown.

In the present study, leveraging on RNA sequencing (RNA-Seq) screening of four different skeletal muscles [transverse abdominal (TA), extensor digitorum longus (EDL), soleus (Sol), and gastrocnemius (Gas)] at different ages, we identified that Tfr1 expression is gradually declined along with ageing in both skeletal muscle and SCs. SC-specific deletion of *Tfr1* leads to decreased regeneration potential, with phenotype of atrophy, iron accumulation, adipocyte biosynthesis, infiltration of macrophages, mitochondrial stress, reduced running ability, and metabolic dysfunction. Gene expression profiling of TA muscle from *Tfr1^{SC/WT}* and *Tfr1^{SC/KO}* mice identifies a group of genes associated with biosynthesis of unsaturated fatty acid, glutathione metabolism, and ferroptosis, which may be associated with the irreversible depletion of SCs, possibly due to up-regulation of Slc39a14, a non-TBI (NTBI) transporter to exacerbate iron-mediated cell death. Moreover, ferrostatin-1 (Ferro-1), a ferroptosis inhibitor, could not rescue the *Tfr1* deletion-induced ferroptosis, unless Tfr1 function was restored by lentivirus. This genetic model also recapitulated one of an unrecognized ageing-related cell death in skeletal muscle with decreased membrane-bound Tfr1 protein but with membrane enrichment of Slc39a14 to uptake NTBI in the skeletal muscle of aged mice. Taken together, our present investigation identified a previously unrecognized function of the Tfr1–Slc39a14–iron axis during skeletal muscle regeneration and ageing, which sheds light on development of novel therapeutic strategies against muscular ageing and diseases.

Methods and materials

Animals

C57BL/6J mice were purchased from the Center of Guangdong Experimental Animal Laboratory and housed in temperature-controlled, humidity-controlled, and ventilated specific pathogen-free cages at animal facility of Guangdong

Institute of Microbiology. All animal handling and procedures were approved by the Animal Care and Use Committee at Guangdong Institute of Microbiology (Permission No. GT-IACUC201704071). All experimental mice were placed on a 12 h/12 h light/dark cycle with *ad libitum* access to food and water.

Mice with *Tfr1*-specific deletion in SCs were generated by crossing mice carrying *Pax7-CreER* and *Tfr1^{fl/fl}* allele. The genotype was *Pax7-CreER^{+/-};Tfr1^{fl/fl}* designated as homozygous (*Tfr1^{SC/KO}*) and *Pax7-CreER^{-/-};Tfr1^{fl/fl}* designated as control littermate (*Tfr1^{SC/WT}*). SC-specific *Tfr1* deletion was generated by intraperitoneal injection of tamoxifen (TMX) (T5648, Sigma, St. Louis, MO) dissolved in corn oil for seven consecutive days at dose of 15 mg/mL as described before.⁹ *Pax7-CreER* mice were shared by Dr Dahai Zhu from Institute of Basic Medical Sciences (Chinese Academy of Medical Sciences), originally purchased from The Jackson Laboratory (Stock No. 017763), and *Tfr1^{fl/fl}* mice were directly purchased from The Jackson Laboratory (Stock No. 028363).

To induce muscle injury, cardiotoxin (CTX, 0.5 nmol, 100 μ L) was intramuscularly administrated. For the drug treatment, CTX-injured mice were intraperitoneally injected with saline or Ferro-1 (2 μ mol/kg, SML0583, Sigma, St. Louis, MO), a ferroptosis inhibitor. For lentivirus administration, mice with CTX-injured TA muscle were intramuscularly administrated with control or lentivirus with Tfr1 expression.

Lentivirus packaging

293T cells seeded in 10 cm plate at 95% confluency were transiently transfected with shuttling vector (pCDH-Tfr1, kindly shared by Dr Fudi Wang or empty vector) and packaging vectors (pVSV-G and psPAX2) by TransIT X2 (MIR60000, Mirus Bio). Twelve hours after transfection, culture medium was replaced with fresh Dulbecco's modified Eagle's medium (DMEM) supplemented with 10% foetal bovine serum (FBS, 01010102, Trinity). Medium containing lentivirus was harvested respectively at 36 and 60 h after transfection. Lenti-X concentrator (PT4421-2, Clontech) was mixed at the ratio of 1:3 and incubated at 4°C for at least 1 h. The mixture was then centrifuged to obtain a high titre virus containing pellet, which was resuspended in 500 μ L ice-cold phosphate-buffered saline (PBS) solution and stored in -80°C freezer for intramuscular injection.

RNA isolation and real-time PCR

Total RNA was extracted with TRIzol™ reagent (1596018, Thermo Fisher, Waltham, MA) and reverse transcribed by utilizing 5X All-In-One MasterMix (G485, AbmGood, Richmond, Canada) according to the manufacturer's instruction. cDNA was used to analyse gene expression by Power SYBR Green

Master Mix (4367659, Thermo Fisher, Waltham, MA) on a QuantStudio 6 Flex Real-Time PCR System (Thermo Fisher, Waltham, MA). The primer sequences for qRT-PCR were listed in Table 1.

RNA sequencing and bioinformatic analysis

Total RNA samples from *C57BL/6J* mice at different ages ($n = 3$ per group) or *Tfr1^{SC/WT}* and *Tfr1^{SC/KO}* ($n = 5$ per group) before and after CTX injury at 30 days after injection (dpi) were sequenced using a BGI-SEQ2000 platform (Beijing Genomics Institute). Bioinformatic analysis was performed as described before.¹³ Raw RNA-seq reads in FASTQ format were quality checked with FASTQC algorithm, and low-quality

reads were trimmed using the FASTX-Toolkit. High-quality reads were aligned to the mouse genome (GRCm38/mm10) using HISAT2 and assembled against mouse mRNA annotation using featureCounts. Differentially expressed genes (DEGs) were analysed by using DESeq2 package in R. Genes were considered to be significantly up-regulated or down-regulated at $padj < 0.05$. Heatmaps were generated using the pheatmap package in R based on raw count of DEGs. Gene ontology analysis was performed using a R package, named clusterProfiler for DEGs (either up-regulated or down-regulated). DEGs ($padj < 0.05$) were further analysed using Gene Set Enrichment Analysis (GSEA). Both up-regulated and down-regulated genes were functionally categorized with the gene ontology and hallmark gene sets as described before.¹³

Table 1 Primer sequence for qPCR

Gene name	Forward primer	Reverse primer
<i>Rps18</i>	CGCCATGTCTCTAGTGATCC	GGTCGATGTCTGCTTTCCTC
<i>Tfr1</i>	TCGTACAGCAGCGGAAGT	TCTCCACGAGCGGAATACAG
<i>Slc11a2</i>	CCAGGATGTGGAGCACCTA	GCTTGTGAACGTGAGGATGG
<i>Slc40a1</i>	TTGTGGCAGGAGAAAACAGG	GCCAATGACTGGAGAACC
<i>Slc39a14</i>	GCTGCTGCTATTTGGGTCTG	GACAAAGGGGACCAGAAAGC
<i>Fth1</i>	GTGCGCCAGAACTACCAC	AGCCACATCATCTCGGTCA
<i>Ftl</i>	CTACCTCTCTGGGCTTCTT	ATGGCCAAGGCAGCTTC
<i>Pax7</i>	TGCCCTCAGTGAGTTCGATT	GAGGTGGGTTCTGATTCCA
<i>MyoD</i>	CGCCACTCCGGGACATAG	GAAGTCGTCTGCTGTCTAAAGG
<i>Cd86</i>	GCCACCCACAGGATCAATTA	TTCGGGTGACCTTGCTTAGA
<i>Cd163</i>	CTCACGGCACTCTTGTTTG	GATCATCCGCTTGAATCCATC
<i>Cd206</i>	CCTTCAGAGGGGTTACCT	TGCCAGGGTCACTTTCA
<i>Col5a3</i>	GATCTCTTGGTCTCGTGAG	CCCAGAGGTCTCTGCAACT
<i>Col6a1</i>	CCTGTGTGAGTGACATG	ATCTGGTGTGGCTGTACTGTA
<i>Col11a2</i>	GACTCTCTGCGGGAGGAG	TCTGTGTGAAGTTGCAG
<i>Col12a1</i>	AGTGCTGGAGCCAGAGG	CCTTCTCTCCAGGCAAACC
<i>Col23a1</i>	ACCGGGAGACTTTGGCC	ATCTTGCCGGGCTCTCC
<i>Adipoq</i>	GTT GGA TGG CAG GCA TCC	AGG AAA GGA GAG CCT GGA G
<i>Fasn</i>	AACCTGGCCATGGTTTTGAG	GCCTGCGCTGTTACATATA
<i>Cd36</i>	TTCAATGGAAAGGATAACATAAGCAAAG	CTGTGCCATTAATCATGTGCGA
<i>Pgc1a</i>	CTCTGGAAGTGCAGGCCTAA	TGCCTGGGTACCAGAACA
<i>Cox7a1</i>	AGCTGCTGAGGACGCA	GTTCTGCTTCTCTGCCAC
<i>Cox8b</i>	TTCCCAAAGCCCATGTCTCT	GGCTAAGACCCATCCTGCT
<i>Ucp1</i>	ATACTGGCAGATGACGTCCC	CGAGTCGCAGAAAAGAAGCC
<i>Cidea</i>	ATACATCCAGCTCGCCCTTT	ACTTACTACCCGGTGTCCAT
<i>Gpx4</i>	CCGGCTACAACGTCAAGTTT	CACGAGCCGTTCTTATCA
<i>Ptgs2</i>	CGGAGAGAGTTCATCCCTGA	GCAGTTTATGTTGTCTGTCCAGA
<i>Hmox1</i>	GAGGTCAAGCACAGGGTGA	CAGGCTCTGACGAAGTGA
<i>Slc3a2</i>	CCAACCTACCAGGGCCAGA	CGTCTGCAACCAAGAACTC
<i>Elovl5</i>	GATGACCAAAGGCCTGAAGC	GGTGGTACCAGTGCAGGA
<i>Elovl6</i>	CTTCGCAAGAACAACCACCA	AGAGGTAGGGACGCATGG
<i>Scd1</i>	ACACCATGGCGTCCAGA	GTTTTCCGCCCTTCTTTGAC
<i>Scd2</i>	AGCAGAATGGAGGCGAGAAG	GGCCCTCATCATCTGATA
<i>Fads1</i>	CACCATGCCAAGCCTAACTG	TGGTGTATGGCATGTGCTTC
<i>Fads2</i>	CAAGCCCAACATCTCCACA	TCATGCTGGTGGTTGTAGG
<i>Dclk1</i>	TGAGCATCCCTGGGTTAATGAT	GAAAGCTTGCCTGCAGTGC
<i>Cd34</i>	CCAGGGTATCTGCCTGGAAC	TCAGCCTCTCTTTTCA
<i>Cd44</i>	TTCGATGGACCGTTACCATAA	AGCTTCTGGGGTGTCTT
<i>Kit</i>	AGAGATTTGGCAGCCAGGA	TCTCTGGTGCATCCACTTC
<i>En1</i>	ACAGCAACCCTAGTGTGG	TACGGGTTTGCCTGGAAC
<i>Ly6a</i>	TCAATTACCTGCCCTACCC	CAGAGGTCTTCTGGCAACA

Iron assay

Skeletal muscle (TA, EDL, Sol, and Gas) non-haem iron (NHI) levels or serum iron levels were determined following a standard protocol. In short, weight skeletal muscles were homogenized in H₂O and equal volume of acid solution (10% trichloroacetic acid in 3 M HCl) added. Samples were digested for 1 h at 100°C; 75 µL digested sample or iron standard was mixed with 75 µL ferrozine solution (1 mM ferrozine, 3 M sodium acetate, and 1% mercaptoacetic acid), followed with incubation at 37°C for 1 h before the colorimetric reading was measured at 565 nm by a microplate photometer (Thermo Fisher, Waltham, MA). The iron level of each sample was normalized by the weight of skeletal muscles and presented as micrograms of iron per gram of wet tissue weight.

Oil Red O staining

Four percent paraformaldehyde (PFA)-fixed TA muscle sections were stained in an Oil Red O solution following a standard protocol. The nuclei were counterstained with haematoxylin before mounted with glycerol-containing mounting medium.

Perls' Prussian blue staining

Non-haem iron staining was performed by utilizing a standard Perl's Prussian blue staining protocol. Images were visualized and captured with a light microscope.

Masson's trichrome staining

Masson's trichrome staining was performed using Masson's Trichrome Stain Kit (Aniline Blue) following the manufacturer's instructions (MA0123, Meilunbio). Briefly, Masson's trichrome staining was performed on 10 µm cryosection of TA muscle fixed with 95% alcohol for 20 min. Sections then were incubated with different solutions supplemented in Masson's Trichrome Stain Kit. At the end, the section was dehydrated with 95% alcohol for 10 s, two rinses in anhydrous alcohol for 10 s, and two rinses in xylene for 1 min each. The sections were mounted with Neutral balsam for imaging and fibrosis quantification. TA muscle fibrosis quantification was performed by using ImageJ. Collagen volume fraction, which was calculated to be the ratio of the collagen-positive blue area vs. the total tissue area.

Haematoxylin and eosin staining

Transverse abdominal sections at 10 µm were stained with haematoxylin and eosin solution. Sections were dehydrated

and mounted with DPX Mountant (44581, Sigma, St. Louis, MO). Histological images were visualized and captured by a light microscope.

Protein isolation and western blot

Total protein lysates were prepared and resolved on sodium dodecyl sulfate–polyacrylamide gel electrophoresis as described before.⁹ Protein band on a polyvinylidene fluoride membrane was probed with primary antibodies (Cav1: D161423 and tubulin: D225847, Sangon Biotech; Tfr1: ab84036 and mitochondrial complex: ab110413, Abcam, Cambridge, United Kingdom; PGC1α: ab3242, Millipore, Burlington, MA; Pparγ: sc-7273, Fth1: sc-376594, and Ftl: sc-74513, Santa Cruz Biotechnology, Dallas, TX; Gpx4: A1933, ABclonal, Wuhan, China; Slc39a14: PA5-21077, Thermo Fisher, Waltham, MA; and Acc: 3676 and Nrf2: 12721, Cell Signaling Technology, Danvers, MA) overnight, followed with secondary antibodies incubation at room temperature (RT) for 1 h. Images were acquired using the ChemiDoc™ Imaging System (Bio-Rad, Hercules, CA).

Myofibre isolation, culture, and immunofluorescence staining

Single myofibres were isolated from EDL muscle following the method as described before.^{9,14} Briefly, EDL muscle was isolated and incubated with digestion medium containing 0.2% collagenase for 75 min. After digestion, myofibres were transferred to a horse serum-coated 24-well plate and gently washed for three times with the washing medium (DMEM supplemented with 10% FBS and 1% penicillin and streptavidin). For non-cultured myofibre, at least 100 myofibres for each group were fixed with 4% PFA (P6148, Sigma, St. Louis, MO), and immunostaining was performed following a standard protocol. For myofibre culture, single myofibre was cultured in either a horse serum-coated 24-well plate (for non-attached culture) or a collagen-coated 24-well plate (for attached culture). In each well, ~20 myofibres were washed for three times before being replaced with culture medium (DMEM supplemented with 20% FBS, 1% penicillin and streptavidin, and 1% chicken embryo extract (C19041654, USBiological, Salem, MA) with or without 4-OH TMX (1 µm, H7904, Sigma, St. Louis, MO). For non-attached culture, after 72 h culture, single myofibres with SC cluster were fixed with 4% PFA, and immunostaining was performed following a standard protocol. For attached culture, after 72 h culture, SC cluster attached the culture plate and proliferated for 4–6 days until reaching 85% confluency, followed by 3 days' differentiation with 2% horse serum. The myotubes were fixed with 4% PFA, followed by immunostaining. Single myofibre or differentiated myotubes

were permeabilized with 0.5% Triton X-100 for 10 min before blocking with sterilized PBS containing 3% bovine serum albumin, 5% goat serum, and 0.5% Tween 20). Primary antibodies (DSHB: Pax7: PAX7, eMyHC: F1.652, MHC:20-s, Abcam, Cambridge, United Kingdom: Tfr1: ab84036 and Active Motif: MyoD: 39991; Ki67: ZM-0167, ZSGB-Bio) were incubated overnight at 4°C and secondary antibodies at RT for 1 h at dark. Myofibres were mounted with DAPI-containing mounting medium (F6057, Sigma, St. Louis, MO). To quantify the number of SCs, Pax7⁺ SCs on myofibres with Tfr1, MyoD, and Ki67 expression were counted. Images were visualized and captured with EVOS Cell Imaging Systems (EVOS FL, Thermo Fisher, Waltham, MA) or Confocal Microscope (Zessie 710).

Cryosection and immunofluorescence staining

Transverse abdominal muscle was dissected, mounted, frozen, and sectioned at 10 µm as described before.⁹ TA muscle section was fixed with 1% PFA, and antigen retrieval was performed with Tris-EDTA buffer (Tris 1.21 g and EDTA 0.37 g dissolved in 1 L ddH₂O, pH 9.0) for 1 h at 100°C. Sections were permeabilized with 0.5% Triton X-100 for 10 min and blocked with blocking buffer (PBS with 3% bovine serum albumin and 5% goat serum) for 1 h. Primary antibodies were incubated overnight at 4°C (wheat germ agglutinin: W32466, Thermo Fisher; LaminB2: 05-206, Millipore; DSHB: Pax7: PAX7, type I: #BA-D5, type IIA: SC-71, type IIB: BF-F3, and type IIX: 6H1-s, perilipin: 9349, Cell Signaling Technology, Danvers, MA), followed by secondary antibodies incubation at RT for 1 h in dark room. Nuclei were counterstained with DAPI-containing mounting medium (F6057, Sigma, St. Louis, MO). The image was visualized and captured with the EVOS Cell Imaging Systems (Thermo Fisher, Waltham, MA).

Transmission electron microscopy

Transverse abdominal muscle injury was induced by intramuscular injection of CTX for both *Tfr1*^{SC/KO} and control littermates; 15 days after injury, TA muscle samples were quickly dissected and immediately fixed in 4% phosphate glutaraldehyde. Each sample was dehydrated, permeabilized, embedded, sectioned at 60–80 nm, and mounted. For each sample, five fields of view were randomly selected and the images were captured.

Treadmill exhaustion test

Treadmill exhaustion test was performed for both *Tfr1*^{SC/KO} and *Tfr1*^{SC/WT} before and after CTX-induced muscle regeneration. The treadmill running protocol was started with an

adaptation period of 10 m/min for 20 min before an increase of 2 m/min every 20 min until fatigue response initiated. The treadmill running protocol was terminated when mice no longer responded to five consecutive fatigue stimuli. Upon fatigue initiation, mice were quickly removed from treadmill running lane. Treadmill running time and distance were recorded and calculated for all mice.

Flow cytometry

Transverse abdominal muscles were dissected, minced, and digested in 0.2% collagenase for 45 min. Single-cell suspensions were incubated with purified anti-CD16/CD32 Abs (clone 2.4G2, Sungene Biotech, Tianjin, China) for 15 min to block Fc receptors. After washing, cells were stained with eFluor 450 anti-mouse CD45 (clone 30-F11, Invitrogen, Carlsbad, CA), Percp-Cy5.5-anti-mouse/human CD11b (clone M1/70, Biolegend, San Diego, CA), PE-Cy7-anti-mouse F4/80 (clone BM8, Biolegend, San Diego, CA), APC-anti-mouse CD86 (clone GL-1, Biolegend, San Diego, CA), FITC-anti-mouse CD206 (clone C068C2, Biolegend), or isotype controls at 4°C for 15 min and detected by flow cytometry (FACSVerse, BD). Data were analysed using FlowJo software (V10). Macrophages were identified as CD45⁺/CD11b⁺/F4/80⁺, and the percentage of pro-inflammatory (CD86⁺) and anti-inflammatory (CD206⁺) macrophages was analysed and shown.

Skeletal muscle biopsy sample collection

The experiment was approved by the Ethics of The Third Affiliated Hospital of Sun Yat-Sen University (Approval No. [2018]02-165-01). Skeletal muscle biopsies were originally collected from patients who experienced fractures followed by clinical treatment and stored in –80°C biobank. Individuals were divided into young (<30 years old) and old group (older than 60 years old), and their skeletal muscle biopsy samples were used for qRT-PCR to determine iron metabolism-related, adipogenesis-related, and ferroptosis-related gene expression.

Statistical analysis

Experiment results were presented as mean ± standard error of the mean. Statistical analysis was performed by GraphPad Prism 7 using unpaired Student's *t*-test or one-way analysis of variance. Differences with a *P* < 0.05 were considered significantly different. Representation of *P*-values was as follows: **P* < 0.05, ***P* < 0.01, ****P* ≤ 0.001, and N.S.: not significant (*P* ≥ 0.05).

Results

Tfr1 expression negatively correlates with skeletal muscle ageing

Skeletal muscle development, growth, and maintaining are precisely regulated physiological processes, without which muscle loss and sarcopenia may occur. To precisely understand these processes, skeletal muscles (TA, EDL, Sol, and Gas) were collected from *C57BL/6J* mice across five different ages (Supporting Information, Figure S1A). RNA-Seq was performed followed by bioinformatic analysis that identified ~5000 DEGs among four different muscles (TA: 5517 genes; EDL: 4583 genes; Sol: 5529 genes; and Gas: 5865 genes) between the young (2 weeks old) and aged (80 weeks old) groups. By plotting expression of these genes across five ages, we identified a clear trend of gene expression pattern, which was divided into two clusters, a gradually increased (Cluster I) and decreased (Cluster II) expression of genes (Figure S1B–S1E). Of these DEGs of four types of muscles, 2445 DEGs were identified, with 1155 up-regulated and 1290 down-regulated genes (Figure 1A). As shown by functional analysis of the gene ontology against the biological process gene set, stem cell proliferation and muscle cell differentiation were down-regulated in TA muscle of the aged group (Figure 1B). More specifically, iron metabolism-related biological function was declined in the aged group, which was also demonstrated by GSEA (Figure 1B and 1C). We also profiled the expression of transition metal ion homeostasis-related genes such as iron, copper, and zinc. Other than cellular iron homeostasis-related genes, copper and zinc ion homeostasis-related genes were partially or less differentially regulated across five different ages (Figure S2A and S2B). Among these iron homeostasis-related genes, *Tfr1* expression was gradually decreased with ageing (from 2 to 8, 30, 60, and even to 80 weeks old) (Figure 1D). qPCR and western blotting also confirmed that *Tfr1* mRNA and protein expression was decreased in four different muscles of 8-week-old mice compared with those for 2-week-old mice, correspondingly accompanied by decreased NHI (Figures 1E and 1F and S2C). *Tfr1* mRNA and protein expression was further decreased in TA muscles of mice with advanced age (Figure S2D and S2E). These data indicate that *Tfr1*-mediated iron absorption is a rate-limiting step in skeletal muscles and may be associated with age-related muscle physiology and function.

Tfr1 is highly expressed in proliferative satellite cells

Satellite cells contribute to not only skeletal muscle development but also postnatal myofibre formation and skeletal muscle regeneration.⁷ However, biological properties of the

Tfr1–iron axis in SCs remain unexplored. Here, by performing single myofibre isolation and immunostaining, we observed that *Tfr1* protein expression level was higher in SCs of 2-week-old mice than that of 8-week-old mice (Figure 1H). Pax7, Ki67, and *Tfr1* immunostaining was performed for single myofibres from both 2- and 8-week-old *C57BL/6J* mice. Approximately 70% of SCs on the myofibres of 2-week-old mice were Ki67⁺, compared with 8-week-old mice that only ~7% of SCs turned into Ki67⁺. *Tfr1* expression level was highly correlated with the level of Ki67 expression in SCs. We quantified *Tfr1* protein expression level into three categories in Pax7⁺ SCs, High, Intermediate (Inter), and Low. Here, both *Tfr1*^{High}/Ki67⁺ and *Tfr1*^{Inter}/Ki67⁺ SCs were the dominant populations in 2-week-old mice, while *Tfr1*^{Low}/Ki67[−] SCs were barely detected. In contrast, it was completely opposite in 8-week-old mice, whereas *Tfr1*^{Low}/Ki67⁺ SCs were the dominant population. In 8-week-old mice, both the *Tfr1*^{High}/Ki67⁺ and *Tfr1*^{Inter}/Ki67⁺ populations remained at low amounts (Figure 1I and 1J). The *Tfr1* protein level was also determined in the SCs of aged mice (~80 weeks old). Compared with 8-week-old mice, *Tfr1* expression was almost undetectable in SCs of aged mice (Figure S3A). These results suggest that *Tfr1* protein level in SCs positively correlates with cell proliferation status but negatively corresponds with skeletal muscle ageing.

Tfr1-mediated iron absorption is indispensable to satellite cell proliferation and differentiation

Tfr1 protein is highly expressed in proliferative cells, while its expression is barely detected in quiescent SCs. To further prove this hypothesis, single myofibres were isolated and cultured *ex vivo* to induce SC proliferation and differentiation. In adult quiescent SCs (Pax7⁺/MyoD[−]), *Tfr1* protein was expressed at low level. However, upon exposure to *ex vivo* culture, *Tfr1* protein level was dramatically induced in activated SCs (Pax7⁺/MyoD⁺, 24, 48, and 72 h after culture) (Figure S3B and S3C). This observation could be due to metabolic alterations during activation and proliferation, which require iron to support mitochondrial energy and glucose metabolism in newly activated SCs. To support the biological effect of iron on SC proliferation and differentiation, single myofibres were cultured with Deferoxamine (DFO) to reduce extracellular iron availability to SCs. Upon 72 h of culture, it resulted in a small cluster size, suggesting that iron is an essential component for SC proliferation (Figure S4A and S4B). Iron chelation also led to poor differentiation and myotube formation (Figure S4C and S4D). Furthermore, gradually increasing intracellular iron also significantly inhibited SC proliferation, cluster formation, differentiation, and fusion to form mature myotubes (Figure S4E–S4H). All of these data indicate that *Tfr1*-mediated iron homeostasis is critical to support myoblast proliferation and differentiation.

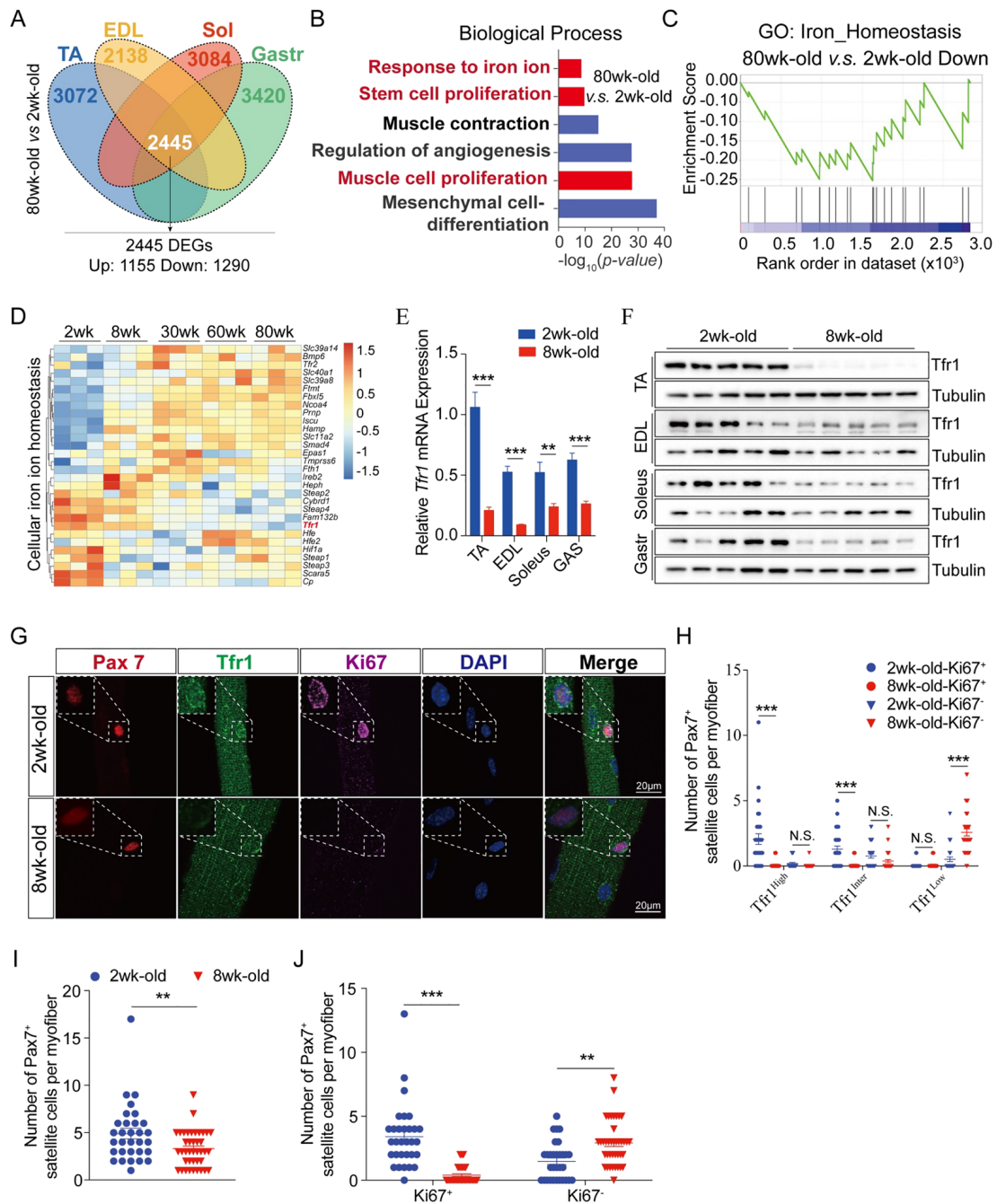


Figure 1 Identification of *Tfr1* as a key biomarker regarding skeletal muscle ageing and satellite cell (SC) activity. (A) Venn diagram showing overlapped genes between young (2 weeks old) and aged (80 weeks old) mice among four types of muscle [transverse abdominal (TA), extensor digitorum longus (EDL), soleus (Sol), and gastrocnemius (Gas)] ($n = 3$ per group). (B) Gene ontology (GO: biological process) analysis against down-regulated genes between 2- and 80-week-old *C57BL/6J* mice. (C) Gene Set Enrichment Analysis (GSEA) analysis of down-regulated pathway in response to the iron homeostasis. (D) Heatmap of cellular iron homeostasis-related gene expression in TA muscle across five different ages (2, 8, 30, 60, and 80 weeks old). (E) qPCR analysis of *Tfr1* expression in four types of skeletal muscles (TA, EDL, Sol, and Gas) between 2- and 8-week-old *C57BL/6J* mice ($n = 5$ per group). (F) Representative western blot image of four types of skeletal muscles (TA, EDL, Sol, and Gas) between 2- and 8-week-old *C57BL/6J* mice ($n = 5$ per group). (G) Representative images of myofibres isolated from 2- and 8-week-old *C57BL/6J* mice ($n > 50$ myofibres from five mice per group). Immunofluorescence of Pax7 (red), *Tfr1* (green), Ki67 (pink), and DAPI (blue) staining revealed that *Tfr1* is highly expressed in SCs at proliferative state (Ki67⁺) for 2-week-old mice but not 8-week-old adult mice. (H) Number of Ki67⁺ and Ki67⁻ SCs with different *Tfr1* expression level (High, Inter, and Low) per myofiber. (I) Number of Pax7⁺ SCs per myofiber. (J) Number of Ki67⁺ and Ki67⁻ SCs per myofiber. N.S., not significant, ** $P < 0.01$, and *** $P < 0.005$, by two-sided Student's *t*-test. Data represent the mean \pm standard error of the mean.

Tfr1 is required for maintaining satellite cell homeostasis

To further understand the biological function of Tfr1 in SCs, SC-specific *Tfr1* knockout mice were generated by crossing mice carrying *Tfr1^{fl/fl}* allele with *Pax7-CreER* transgenic mice. The genotype of experimental mice was *Pax7-CreER;Tfr1^{fl/fl}*. *Tfr1-KO* mice and control littermates were denominated as *Tfr1^{SC/KO}* and *Tfr1^{SC/WT}*, respectively. The deletion was induced by intraperitoneal injection of TMX for seven consecutive days as described before.⁹ Single myofibre isolation from EDL muscle of *Tfr1^{SC/WT}* and *Tfr1^{SC/KO}* mice was performed, followed by immunostaining of Pax7, MyoD, and Tfr1. Seven days after injection of TMX, the number of Pax7⁺ SCs was decreased in *Tfr1^{SC/KO}* compared with that of *Tfr1^{SC/WT}* (Figure 2A–2C). Meanwhile, SCs with ablation of *Tfr1* did not express Ki67 or MyoD, indicating that *Tfr1* deletion did not lead to SC activation (Figure 2A–2C). Furthermore, the number of SC on a single myofibre was counted after TMX injection (1, 4, 7, 10, 14, 21, and 30 dpi). Short term of TMX injection (1 and 4 dpi) did not change the number of SCs dramatically, while the number of SCs gradually decreased since 7 dpi of TMX (Figure 2D). Deletion of *Tfr1* in SCs blocks TBI absorption, which may cause an irreversible and cell-autonomous defect of SCs. To test this hypothesis, single myofibres from either *Tfr1^{SC/WT}* or *Tfr1^{SC/KO}* mice were cultured in horse serum-coated plates (flowing culture) or collagen-coated plates (attached culture) in the presence of 4-OH TMX. TMX-induced deletion of *Tfr1* inhibited SC activation, proliferation, and differentiation, as demonstrated by significantly decreased number of clusters, reduced number of SCs in each cluster, failed myotube formation, and a lower fusion index (Figure 2E–2H). *Tfr1* deletion inhibiting myoblast proliferation and differentiation was further tested in myoblasts bearing floxed *Tfr1* allele, whereas its deletion was induced by adenovirus expressing Cre recombinase. Both control and Cre-expressing adenovirus-infected myoblasts were incubated with EdU-containing medium (10 μM) for 24 h. The incorporation of EdU was significantly lower in the *Tfr1* deleted group (20%) than that in the control group (60%) (Figure S5A–S5D). The biological function of Tfr1 was also confirmed in C2C12 myoblasts via either gRNA-mediated or siRNA-mediated *Tfr1* knockdown. As shown in C2C12 myoblasts, similar to the observation of SCs on single myofibre, *Tfr1* deletion inhibited C2C12 myoblast differentiation (Figure S6A–S6H).

Tfr1 deletion impairs skeletal muscle regeneration

To understand the biological function of Tfr1 in skeletal muscle growth and regeneration, we utilized adult mice with conditional ablation of *Tfr1* in SCs. Seven days after injection of TMX, TA muscle was injured by intramuscular injection of

CTX and harvested for further analysis upon completion of regeneration (30 dpi, Figure 3A). We observed a poor regeneration with *Tfr1* ablation in SCs, showing a muscular atrophy but obviously no change on body weight (Figure 3B and 3C). To assess the biological function of Tfr1 during TA muscle regeneration, the number of Pax7⁺ SCs and eMyHC⁺ myotubes (newly formed myotubes) was counted. Upon CTX-induced injury (5 and 9 dpi), Pax7⁺ SCs were highly proliferated in *Tfr1^{SC/WT}* mice, while they were barely detected in *Tfr1^{SC/KO}* mice on TA muscle sections (Figure 3D and 3E). Low SC numbers were further confirmed by *Pax7* mRNA expression indicating that *Tfr1* deletion led to depletion of Pax7⁺ SCs upon skeletal muscle injury (Figure S7A). *Tfr1* KO in SCs also decreased eMyHC⁺ myotube formation at 5 dpi (Figure 3F) while there was a slightly increase in eMyHC⁺ myotubes at 9 dpi (Figure 3G), which may be due to a robust induction of myogenic transcription factor, *MyoD* expression (Figure S7A). Upon the completion of regeneration, ablation of *Tfr1* resulted in nearly complete depletion of SCs, followed by atrophy and fibrosis (Figures 3H–3J and S7B–S7E).

Tfr1 in satellite cells is essential to maintain skeletal muscle micro-environment and regeneration

To precisely understand how SC-specific knockout of *Tfr1* affects the skeletal muscle micro-environment, RNA-Seq was performed to assess gene expression profile in TA muscle between *Tfr1^{SC/WT}* and *Tfr1^{SC/KO}* mice before or after injury. Approximately 8478 DEGs were identified among four groups (Figure S8A). Gene clustering and principal coordinate analysis (PCoA) showed that *Tfr1^{SC/KO}* mice with CTX injection exhibited a distinct molecular signature from the other three groups, which had similar molecular signatures (Figure 4B). Thus, we focused on DEGs and functional enrichment between *Tfr1^{SC/WT}* and *Tfr1^{SC/KO}* mice after CTX-induced injury. Among DEGs, 3596 genes were up-regulated, while 4882 genes were down-regulated (Figure 4C). Gene ontology analysis (biological process) identified genes that were majorly involved in dysregulation of immune balancing and metabolic homeostasis. This was represented by up-regulated genes that were associated with macrophage activation, macrophage-derived foam cell differentiation, lipid biosynthetic process, and collagen biosynthetic process, while down-regulated genes were involved in mitochondrial respiration chain complex assembly, tricarboxylic acid cycle, muscle cell differentiation, and fatty acid β-oxidation (Figures 4D and S8B–S8E). The enriched biological functions were further confirmed by GSEA (Figure 4E and 4H). Here, we found that in regenerated TA muscle, *Tfr1* knockout resulted in macrophage infiltration, which was assessed by flow cytometry via detecting M1 (0.17% vs. 0.012%) and M2 (0.88% vs. 8.72E⁻³%) macrophages by their membrane

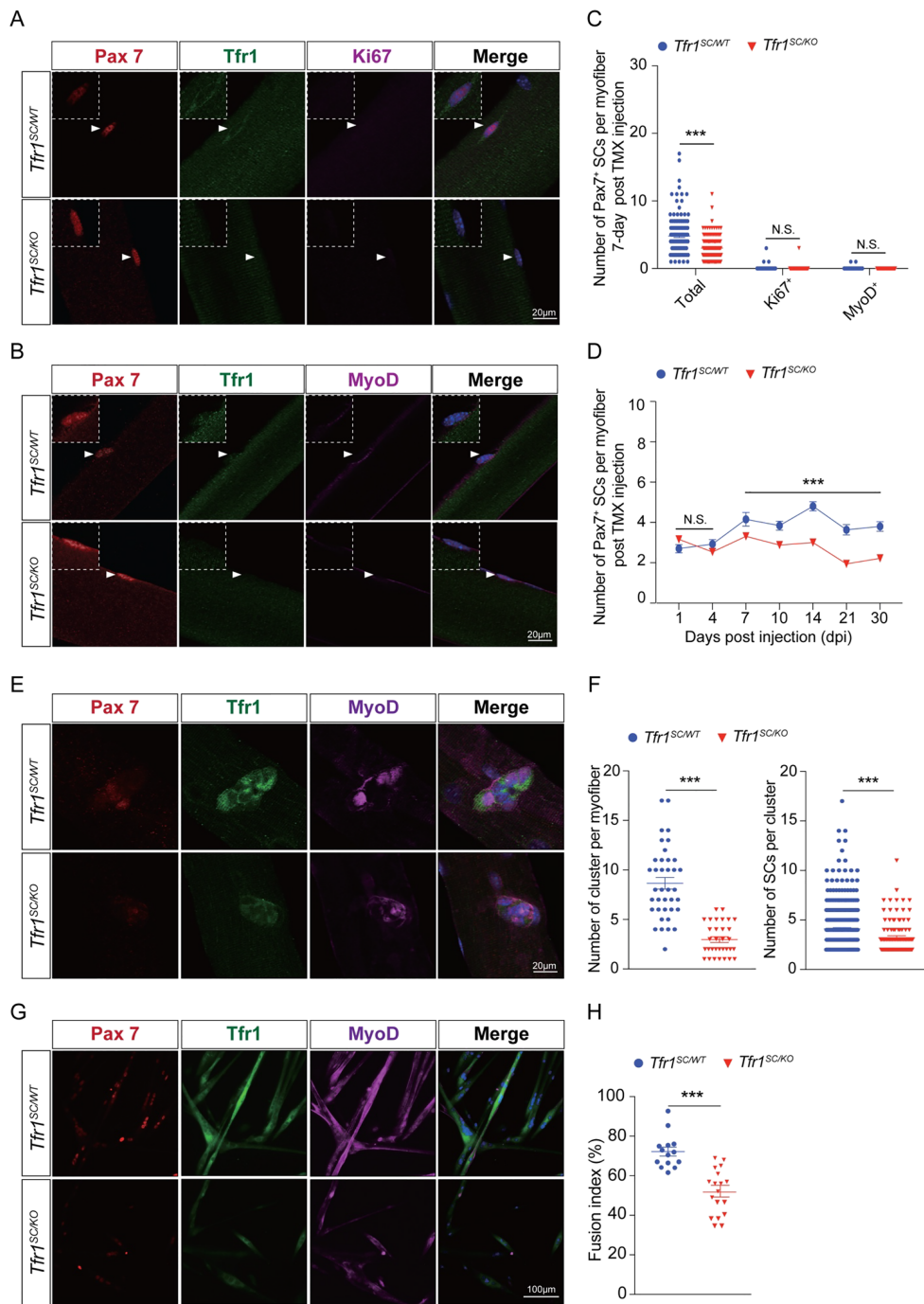


Figure 2 Genetic deletion of *Tfr1* in quiescent satellite cells (SCs) abolishes the activation, proliferation, and differentiation. (A) Representative images of myofibres isolated from *Tfr1^{SC/WT}* and *Tfr1^{SC/KO}* mice ($n > 50$ myofibres from five mice per group). Immunofluorescence of Pax7 (red), Tfr1 (green), Ki67 (pink), and DAPI (blue) staining. (B) Representative images of myofibres isolated from *Tfr1^{SC/WT}* and *Tfr1^{SC/KO}* mice ($n > 50$ myofibres from five mice per group). Immunofluorescence of Pax7 (red), Tfr1 (green), MyoD (pink), and DAPI (blue) staining. (C) Number of total, Ki67⁺, and MyoD⁺ SCs per myofiber between *Tfr1^{SC/WT}* and *Tfr1^{SC/KO}* mice. (D) Both *Tfr1^{SC/WT}* and *Tfr1^{SC/KO}* mice were administered with tamoxifen (TMX) on the same day. Number of Pax7⁺ SCs per myofiber was calculated at 1, 4, 7, 10, 14, 21, and 30 days after TMX-induced *Tfr1* deletion ($n = 5$ mice per group per time point). (E) Representative images of SC clusters on myofiber from *Tfr1^{SC/WT}* and *Tfr1^{SC/KO}* mice *ex vivo* cultured for 72 h ($n > 50$ myofibres from seven mice per group). Immunofluorescence of Pax7 (red), Tfr1 (green), MyoD (pink), and DAPI (blue) staining ($n > 20$ myofibres from seven mice per group). (F) Number of SC clusters per myofiber and number of Pax7⁺ SCs per cluster ($n > 50$ myofibres from five mice per group). (G) Representative images of differentiated myotubes from SCs on myofiber isolated from *Tfr1^{SC/WT}* and *Tfr1^{SC/KO}* mice ($n > 10$ myofibres from five mice per group). (H) Summary of fusion index of SCs on myofiber differentiated in Dulbecco's modified Eagle's medium supplemented with 2% horse serum ($n > 10$ myofibres from five mice per group). N.S., not significant, and *** $P < 0.005$, by two-sided Student's *t*-test. Data represent the mean \pm standard error of the mean.

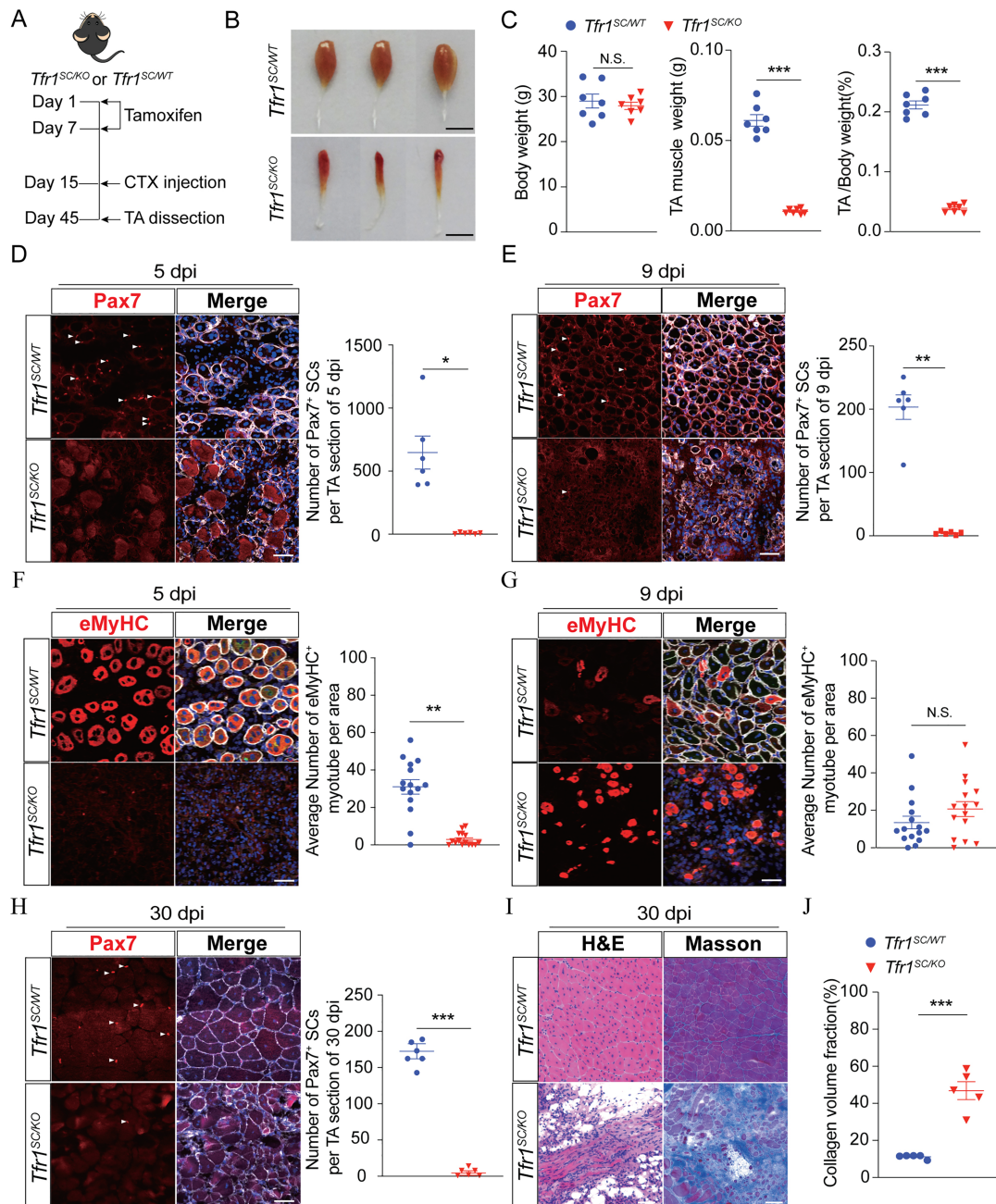


Figure 3 *Tfr1* ablation in satellite cells (SCs) delays skeletal muscle regeneration. (A) Timeline characterizing skeletal muscle regeneration upon tamoxifen-induced *Tfr1* ablation in SCs. (B) Representative image of transverse abdominal (TA) muscle upon completion of regeneration between *Tfr1*^{SC/WT} and *Tfr1*^{SC/KO} mice at 30 dpi. (C) Summary of body weight, TA muscle weight, and ratio of TA muscle and body weight between *Tfr1*^{SC/WT} and *Tfr1*^{SC/KO} mice upon completion of regeneration at 30 dpi ($n = 7$ per group). (D) Representative images of TA muscle section from *Tfr1*^{SC/WT} and *Tfr1*^{SC/KO} mice ($n = 6$ mice per group). Immunofluorescence of Pax7 revealed a decrease in the number of Pax7⁺ SCs (arrowheads) and number of Pax7⁺ SCs per TA muscle section at 5 dpi (right of immunostaining images). (E) Representative images of TA muscle section from *Tfr1*^{SC/WT} and *Tfr1*^{SC/KO} mice ($n = 6$ mice per group). Immunofluorescence of Pax7 revealed a decrease in the number of Pax7⁺ SCs (arrowheads) and number of Pax7⁺ SCs per TA muscle section at 9 dpi (right of immunostaining images). (F) Immunofluorescence of eMyHC⁺ myotubes after cardiotoxin (CTX) injury (5 dpi) and number of eMyHC⁺ myotubes per TA muscle section area at 5 dpi (right of immunostaining images). (G) Immunofluorescence of eMyHC⁺ myotubes after CTX injury (5 dpi) and number of eMyHC⁺ myotubes per TA muscle section area at 9 dpi (right of immunostaining images). (H) Immunofluorescence of Pax7 revealed a decrease in the number of Pax7⁺ SCs (arrowheads) and number of Pax7⁺ SCs per TA muscle section at 30 dpi (right of immunostaining images, $n = 6$ mice per group). (I) Representative images of TA muscles from *Tfr1*^{SC/WT} and *Tfr1*^{SC/KO} mice with haematoxylin and eosin staining and Masson staining upon completion of CTX-induced regeneration (30 dpi, $n = 6$ mice per group). (J) Summary of collagen volume fraction between *Tfr1*^{SC/WT} and *Tfr1*^{SC/KO} mice completion of CTX-induced regeneration at 30 dpi. N.S., not significant, * $P < 0.05$, ** $P < 0.01$, and *** $P < 0.005$, by two-sided Student's *t*-test. Data represent the mean \pm standard error of the mean.

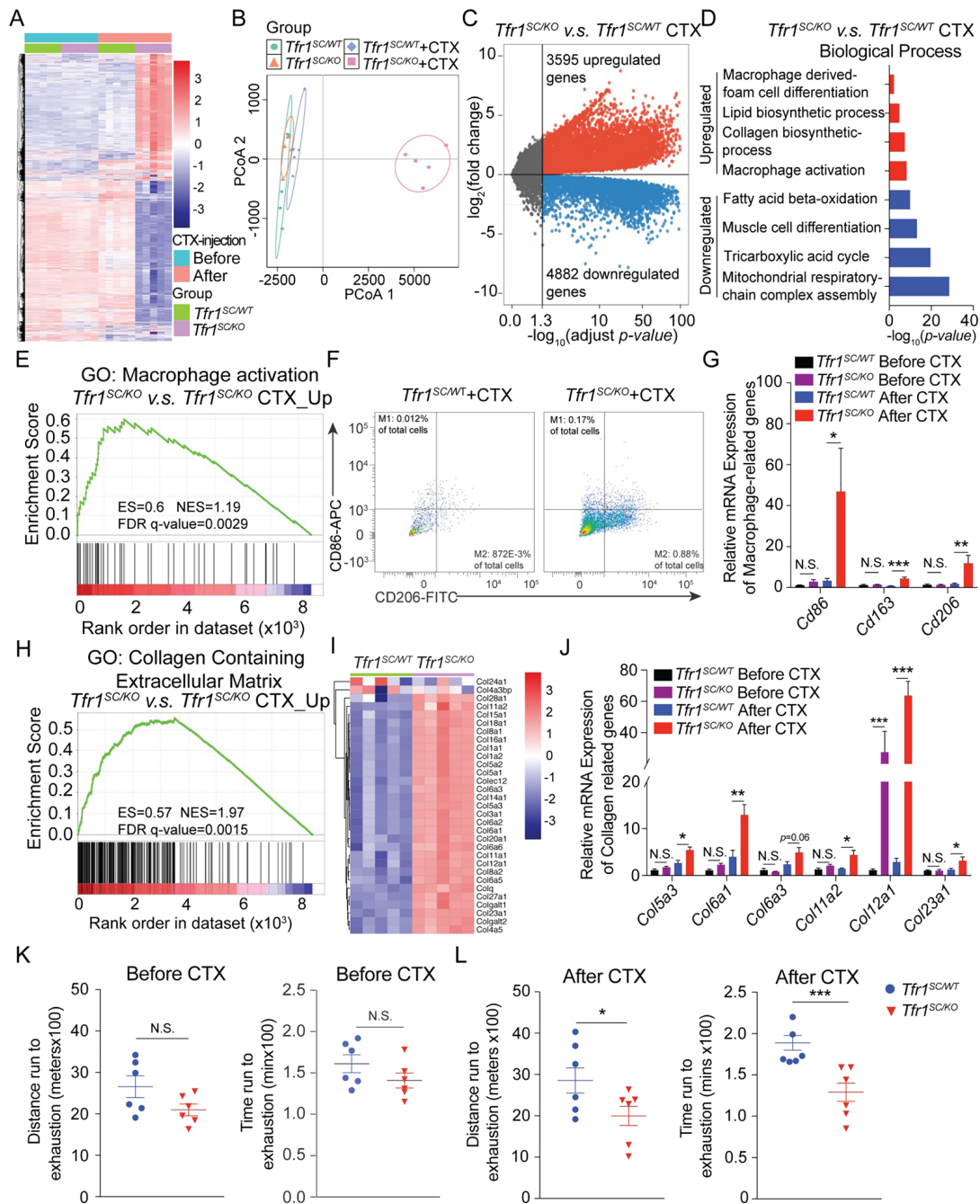


Figure 4 Satellite cell (SC) *Tfr1* deletion in transverse abdominal (TA) muscle of *Tfr1^{SC/KO}* mice results in skeletal muscle dysfunction. (A) Heatmap of mRNA expression profile in TA muscle from adult *Tfr1^{SC/WT}* and *Tfr1^{SC/KO}* mice before or after cardiotoxin (CTX)-induced regeneration at 30 dpi ($n = 5$ per group). (B) Principal coordinate analysis (PCoA) of transcriptome from TA muscle in adult *Tfr1^{SC/WT}* and *Tfr1^{SC/KO}* mice before or after CTX-induced regeneration ($n = 5$ per group). (C) Volcano plot of differentially expressed genes in TA muscle from adult *Tfr1^{SC/WT}* and *Tfr1^{SC/KO}* mice after CTX-induced regeneration. (D) Gene ontology (GO) (biological process) analysis of differentially expressed genes (DEGs) for both up-regulated and down-regulated genes. (E) Gene Set Enrichment Analysis (GSEA) analysis of macrophage activation pathway between *Tfr1^{SC/WT}* and *Tfr1^{SC/KO}* mice upon CTX-induced regeneration at 30 dpi. (F) Flow cytometry analysis of the percentage of CD206⁺/CD86⁺ macrophage in total cells obtained from TA muscle of *Tfr1^{SC/WT}* and *Tfr1^{SC/KO}* mice after CTX-induced injury at 30 dpi. (G) qPCR analysis of *Cd86*, *Cd163*, and *Cd206* mRNA expression in TA muscle from adult *Tfr1^{SC/WT}* and *Tfr1^{SC/KO}* mice before or after CTX-induced injury ($n = 5$ per group). (H) GSEA analysis of collagen-containing extracellular matrix pathway between *Tfr1^{SC/WT}* and *Tfr1^{SC/KO}* mice upon CTX-induced regeneration at 30 dpi. (I) Heatmap for collagen matrix related gene expression profile between *Tfr1^{SC/WT}* and *Tfr1^{SC/KO}* mice after CTX-induced injury at 30 dpi ($n = 5$). (J) qPCR analysis of *Col5a3*, *Col6a1*, *Col6a3*, *Col11a2*, *Col12a1*, and *Col23a1* mRNA expression in TA muscle from adult *Tfr1^{SC/WT}* and *Tfr1^{SC/KO}* mice before or after CTX-induced injury at 30 dpi ($n = 5$ per group). (K, L) Treadmill running distance and running time to exhaustion for *Tfr1^{SC/WT}* and *Tfr1^{SC/KO}* mice before and after regeneration at 30 dpi. N.S., not significant, * $P < 0.05$, ** $P < 0.01$, and *** $P < 0.005$, by two-sided Student's *t*-test. Data represent the mean \pm standard error of the mean.

markers, for example, Cd86, Cd206, and Cd163 (Figure 4F). *Cd86*, *Cd206*, and *Cd163* mRNA expression was also robustly increased only in regenerated TA muscle of *Tfr1^{SC/KO}* mice but not in other groups (Figure 4G). Defective muscle regeneration was also accompanied by extracellular collagen biosynthesis accumulation, with the up-regulation of collagen biosynthesis and accumulation-related genes (Figures 4I–4L and S8C). This may further interrupt exercise activity through reduced running time and distance (Figure 4K and 4L).

Tfr1 deletion in satellite cells leads to the dysregulation of lipid and iron metabolism in skeletal muscle

Satellite cell-specific deletion of *Tfr1* results in dysregulation of local lipid and energy metabolism (Figure 4D). GSEA analysis further confirmed that adipogenesis indeed occurred in the TA muscle of *Tfr1^{SC/KO}* mice (Figure 5A). Adipogenesis-related genes such as *Fasn* and *Adipoq* were significantly induced. However, the expression of the fatty acid uptake gene, *Cd36* expression, was not changed, indicating that a local *de novo* lipogenesis instead of external fatty acid uptake contributed to the lipid accumulation in TA muscle of *Tfr1^{SC/KO}* mice (Figure 5B). Lipid accumulation was visualized by Oil Red O staining and immunofluorescent staining of perilipin and laminin B2. On TA muscle cryosection, a large amount of lipid droplets as well as perilipin⁺ areas were observed only on TA muscle sections of *Tfr1^{SC/KO}* mice but not for *Tfr1^{SC/WT}* mice at 30 dpi (Figure 5C). Other than dysregulation of genes associated with lipid metabolism, most mitochondrial thermogenesis and iron metabolism-related genes were dysregulated, such as *Pgc1α*, *Cox7a1*, and *Cox8b* for mitochondrial thermogenesis and *Tfr1*, *Slc11a2*, *Slc40a1*, and *Fth1* for iron metabolism, except for a moderate up-regulation of *Ftl* (Figure 5D). In contrast, atrophied skeletal muscle of *Tfr1^{SC/KO}* mice had a large amount of labile iron accumulation (Figure 5E). Furthermore, consistent with mitochondrial gene expression, transmission electron microscopy revealed swollen mitochondria with irregular or absent cristae (Figure 5E).

Tfr1 deletion activates ferroptosis in skeletal muscle upon muscular regeneration

Regenerated skeletal muscle of *Tfr1^{SC/KO}* mice presented enhanced adipogenesis and iron accumulation in TA muscle. To profile new gene candidates associated with muscular dysfunction in *Tfr1^{SC/KO}* mice at 30 dpi, we discovered that a group of ferroptotic genes was dysregulated (e.g. *Gpx4*, *Slc7a11*, *Acs14*, and *Hmox1*), along with the KEGG pathway enrichment, including ferroptosis, biosynthesis of

unsaturated fatty acid, and glutathione metabolism (Figure 5F and 5G). Consistent with previous observations in ferroptosis, *Gpx4*, a glutathione-dependent peroxidase was down-regulated, and *Ptgs2* (cyclooxygenase 2), an enzyme converting arachidonic acid to prostaglandin endoperoxide H₂, was up-regulated (Figure 5H). The activation of ferroptosis in skeletal muscle was further confirmed by measuring selective biomarker expression levels. This was shown by increased protein levels of *Acc* and *Pparγ* and the decreased protein levels of *Tfr1*, *PGC1α*, *Nrf2*, *Gpx4*, and *Fth1*, leading to the observation of adipogenesis and dysregulated iron metabolism, respectively, contributing to the activation of ferroptosis. Meanwhile, along with decreased *Gpx4* protein level, total GSH levels in *Tfr1^{SC/KO}* mice were reduced in the TA muscle of *Tfr1^{SC/WT}* mice, which may be due to the decreased expression of *Slc7a11* (Figures 5F and S9A–S9C). Furthermore, along with decreased GSH level, regenerated TA muscle of *Tfr1^{SC/KO}* mice had higher ferroptosis end-product malondialdehyde (MDA), suggesting increased levels of lipid peroxidation (Figure S9D). Further analysis demonstrated that the activation of unsaturated fatty acid biosynthesis pathway contributed to accumulation of lipid in TA muscle of *Tfr1^{SC/KO}* mice (Figure 5J and 5K). The critical enzymes in the unsaturated fatty acid biosynthesis pathway, for example, *Fasn*, *Elvol5*, *Scd1*, *Scd2*, *Fads1*, and *Fads2*, were up-regulated, followed by accumulation of saturated and unsaturated fatty acids (Figures 5L and 5M and S9E–S9G).

Ferroptosis impairs muscular regeneration

To map the time point of ferroptosis occurrence, injured TA muscle from *Tfr1^{SC/WT}* and *Tfr1^{SC/KO}* mice at different time points (5, 9, and 15 dpi) was assessed (Figure 6A). The TA muscle/body weight, as well as *Gpx4*, *Slc3a2*, and *Ptgs2* expression, was not significantly different between *Tfr1^{SC/WT}* and *Tfr1^{SC/KO}* mice at 5 dpi (Figures 6B and S10A–S10G). However, the expression of iron homeostasis-related genes, such as *Slc11a2*, *Slc39a14*, *Fth1*, and *Ftl*, was highly up-regulated at 5 dpi in *Tfr1^{SC/KO}* mice, suggesting that increased iron absorption may occur as early as at 5 dpi (Figure S10A–S10G). Starting at 9 dpi, TA muscle/body weight started to decrease, followed by down-regulation of *Gpx4* and up-regulation of *Ptgs2*, *Slc39a14*, and *Hmox1* expression, so as to those in TA muscle at 15 dpi, except for decreased *Fth1* expression that is associated with oxidization of ferrous iron and iron storage inside ferritin (Figures 6B and S10A–S10G). Iron accumulation and lipid droplets could be observed in the TA muscle of *Tfr1^{SC/KO}* mice starting at 9 dpi (Figure 6C). During muscle regeneration, labile iron in regenerative TA muscle was derived from increased NHI absorption possibly via *Slc39a14* and recycled iron from myoglobin from dead muscle cells but failed to be utilized upon muscular regeneration defect.

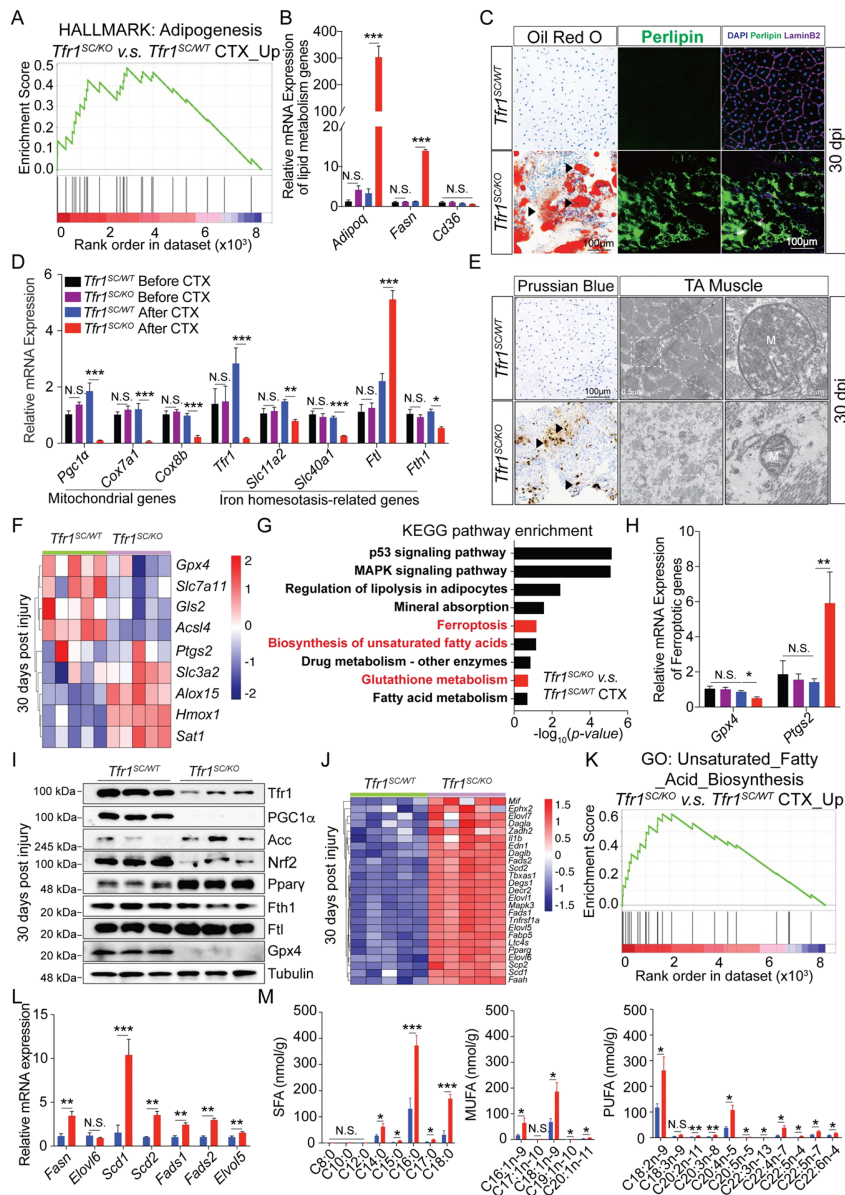


Figure 5 Dysregulation of lipid and iron metabolism activates ferroptosis in injured transverse abdominal (TA) muscle of *Tfr1^{SC/KO}* mice. (A) Gene Set Enrichment Analysis (GSEA) analysis of adipogenesis pathway between *Tfr1^{SC/WT}* and *Tfr1^{SC/KO}* mice upon cardiotoxin (CTX)-induced regeneration at 30 dpi. (B) qPCR analysis of *Adipoq*, *Fasn*, and *Cd36* mRNA expression in TA muscle from adult *Tfr1^{SC/WT}* and *Tfr1^{SC/KO}* mice before or after CTX-induced injury ($n = 5$ per group). (C) Representative images of TA muscle sections from *Tfr1^{SC/WT}* and *Tfr1^{SC/KO}* mice upon CTX-induced injury at 30 dpi ($n = 5$ per group). Oil Red O (ORO) staining and perilipin (green) and laminin B2 (pink) immunofluorescent staining revealed adipogenesis and lipid accumulation in TA muscle of *Tfr1^{SC/KO}* mice. (D) qPCR analysis of *Pgc1α*, *Cox7a1*, and *Cox8b* (mitochondrial genes), *Tfr1*, *Slc11a2*, *Slc40a1*, *Ftl*, and *Fth1* (iron homeostasis-related genes) mRNA expression in TA muscle from adult *Tfr1^{SC/WT}* and *Tfr1^{SC/KO}* mice before or after CTX-induced injury ($n = 5$ per group). (E) Representative images of TA muscle section with Prussian blue staining ($n = 5$ per group) and transmission electron microscope images for TA muscle section from adult *Tfr1^{SC/WT}* and *Tfr1^{SC/KO}* mice after CTX-induced injury at 30 dpi. (F) Heatmap of ferroptosis-related gene expression in TA muscle from adult *Tfr1^{SC/WT}* and *Tfr1^{SC/KO}* mice after CTX-induced injury at 30 dpi ($n = 5$ per group). (G) KEGG pathway enrichment analysis of up-regulated genes in TA muscle from adult *Tfr1^{SC/WT}* and *Tfr1^{SC/KO}* mice after CTX-induced injury at 30 dpi. (H) qPCR analysis of *Gpx4* and *Ptgs2* expression in TA muscle of adult *Tfr1^{SC/WT}* and *Tfr1^{SC/KO}* mice before or after CTX-induced injury ($n = 5$ per group). (I) Representative western blot images of TA muscle between *Tfr1^{SC/WT}* and *Tfr1^{SC/KO}* mice after CTX-induced injury at 30 dpi. (J) Heatmap of unsaturated fatty acid biosynthesis-related gene expression in TA muscle from adult *Tfr1^{SC/WT}* and *Tfr1^{SC/KO}* mice after CTX-induced injury at 30 dpi ($n = 5$ per group). (K) GSEA analysis of unsaturated fatty acid biosynthesis pathway between *Tfr1^{SC/WT}* and *Tfr1^{SC/KO}* mice upon CTX-induced regeneration at 30 dpi. (L) qPCR analysis of *Fasn*, *Elovl5*, *Elovl6*, *Scd1*, *Fads1*, and *Fads2* expression in TA muscle of adult *Tfr1^{SC/WT}* and *Tfr1^{SC/KO}* mice after CTX-induced injury at 30 dpi ($n = 5$ per group). (M) Saturated fatty acid (SFA), monounsaturated fatty acid (MUFA), and polyunsaturated fatty acid (PUFA) levels (nmol/g) in TA muscle of adult *Tfr1^{SC/WT}* and *Tfr1^{SC/KO}* mice after CTX-induced injury at 30 dpi ($n = 4$ per group). N.S., not significant, * $P < 0.05$, ** $P < 0.01$, and *** $P < 0.005$, by two-sided Student's *t*-test. Data represent the mean \pm standard error of the mean.

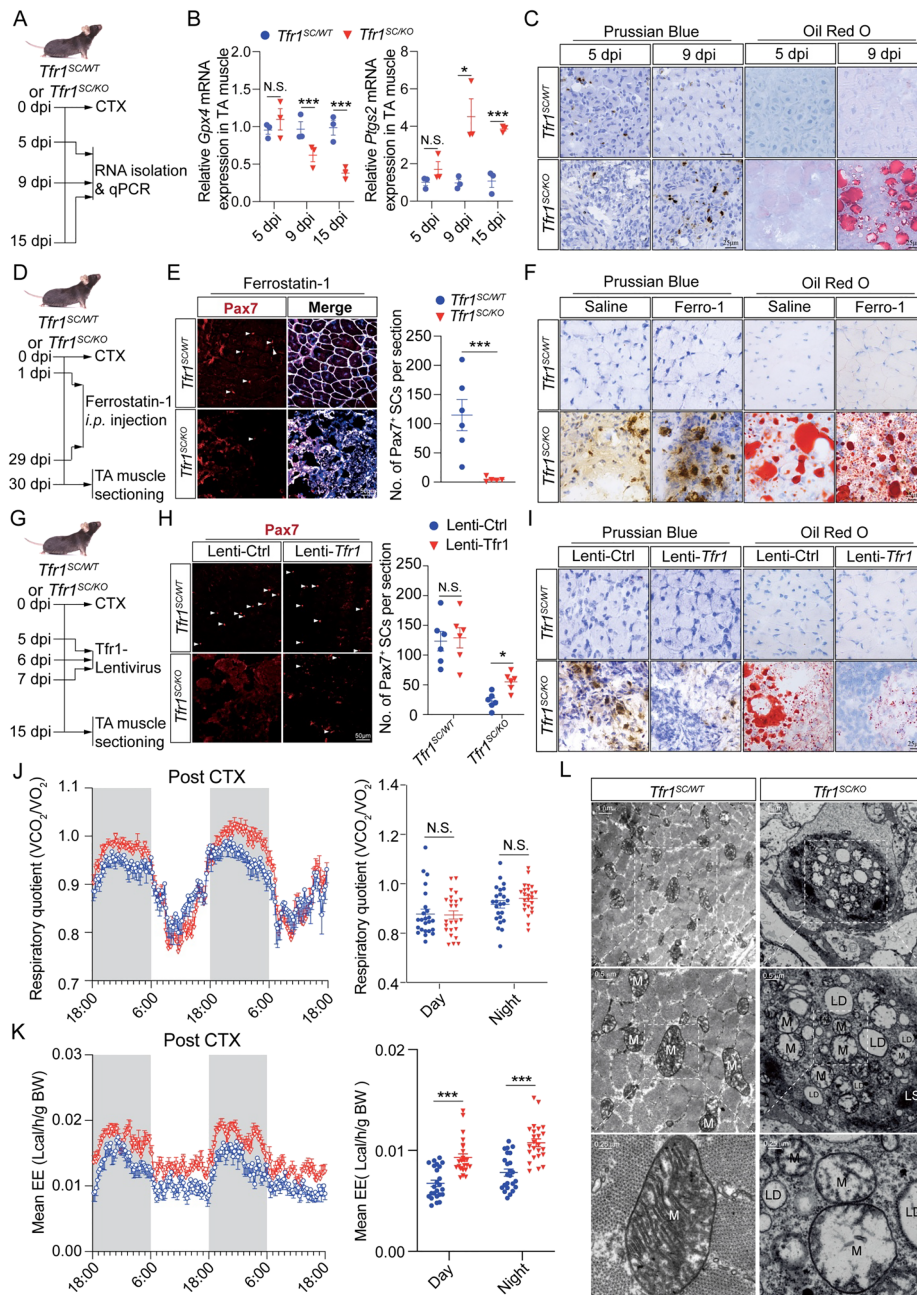


Figure 6 Ferroptosis in transverse abdominal (TA) muscle of *Tfr1^{SC/KO}* mice prevents skeletal muscle regeneration. (A) Timeline characterizing the activation of ferroptosis in TA muscle of *Tfr1^{SC/WT}* and *Tfr1^{SC/KO}* mice after cardiotoxin (CTX)-induced injury. (B) qPCR analysis of *Gpx4* and *Ptgs2* expression in TA muscle from adult *Tfr1^{SC/WT}* and *Tfr1^{SC/KO}* mice after CTX-induced injury at 5, 9, and 15 dpi. (C) Representative images of TA muscle section with Prussian blue and Oil Red O (ORO) staining from *Tfr1^{SC/WT}* and *Tfr1^{SC/KO}* mice after CTX-induced injury at 5 and 9 dpi. (D) Timeline characterizing the effect of ferrostatin-1 to inhibit ferroptosis in TA muscle from *Tfr1^{SC/WT}* and *Tfr1^{SC/KO}* mice. (E) Representative images of TA muscle section immunostaining for Pax7 (red) and laminin B2 (white). Number of Pax7⁺ SCs per section (right) ($n = 6$ per group). (F) Representative images of TA muscle section with Prussian blue and ORO staining from adult *Tfr1^{SC/WT}* and *Tfr1^{SC/KO}* mice after CTX-induced injury between saline and ferrostatin-1 intraperitoneal injection at 30 dpi. (G) Timeline characterizing the effect of lenti-Tfr1 to inhibit ferroptosis in TA muscle from *Tfr1^{SC/WT}* and *Tfr1^{SC/KO}* mice. (H) Representative images of TA muscle section immunostaining for Pax7 (red) and laminin B2 (white) between lenti-Ctrl and lenti-Tfr1 intramuscular injection at 30 dpi. Number of Pax7⁺ SCs per section (right) ($n = 6$ per group). (I) Representative images of TA muscle section with Prussian blue and ORO staining from adult *Tfr1^{SC/WT}* and *Tfr1^{SC/KO}* mice after CTX-induced injury between lenti-Ctrl and lenti-Tfr1 intramuscular injection at 15 dpi. (J) Respiratory exchange rate (VCO_2/VO_2) and energy expenditure were monitored over a 48 h period for *Tfr1^{SC/WT}* and *Tfr1^{SC/KO}* mice after CTX-induced injury at 15 dpi ($n = 8$ mice per group). (L) Representative transmission electron microscope image of TA muscle samples from adult *Tfr1^{SC/WT}* and *Tfr1^{SC/KO}* mice after CTX-induced injury at 30 dpi. N.S., not significant, * $p < 0.05$, and *** $p < 0.005$, by two-sided Student's *t*-test. Data represent the mean \pm standard error of the mean.

Next, we asked whether administration of a ferroptosis inhibitor could rescue the ferroptosis-induced muscular atrophy. Ferro-1, a ferroptosis inhibitor to eliminate lipid peroxidation, was intraperitoneally injected upon intramuscular administration of CTX to TA muscle for 30 consecutive days (Figure 6D). Unfortunately, Ferro-1 did not rescue ferroptosis-induced SC/muscle cell death or reduce labile iron accumulation and lipid droplet formation (Figure 6E and 6F), possibly due to cell-autonomous inactivation, proliferation, and differentiation defects upon *Tfr1* ablation in SCs. Instead, administration of lentivirus-expressing mouse Tfr1 protein could partially reverse ferroptosis-induced SC/muscle cell death by decreasing the labile iron accumulation and lipid biosynthesis (Figure 6G–6I).

Metabolic adaptation of ferroptosis via mitochondrial stress in skeletal muscle

Skeletal muscle-specific deletion of *Tfr1* leads to growth retardation and systemic metabolic disorder (lipid and amino acid) in both muscle and liver.¹⁰ However, for our model, data from mice kept in metabolic cages presented a significantly higher energy expenditure (EE) for *Tfr1*^{SC/KO} mice than that of *Tfr1*^{SC/WT} mice but no difference in the ratio of O₂ consumption and CO₂ production, meaning that an adaptive alteration of systemic metabolism, especially the induction of EE, was probably not due to the change in substrate preference and/or whole-body fuel metabolism (Figure 6J and 6K). Through the transmission electron microscopy, we observed a lysosomal structure containing dead mitochondria (M) without any cristae structure and lipid droplets (LD) in *Tfr1*^{SC/KO} mice (Figure 6L), with higher levels of Fgf21 but lower levels of Trp53 and mitochondrial complex protein (Complexes I, II, III, and V) in the TA muscle of *Tfr1*^{SC/KO} mice (Figure S10H). Increased Fgf21 protein may be due to mitochondrial stress.¹⁵ To eliminate potential endocrinological regulation of systemic metabolism and thermogenesis by Fgf21, iron metabolism-related and thermogenesis-related genes were determined in liver, iBAT, iWAT, and eWAT, showing that no difference in their gene expression between *Tfr1*^{SC/WT} and *Tfr1*^{SC/KO} mice was detected (Figure S11A–S11H). However, Glut4 protein levels were significantly induced in both iWAT and eWAT but not in iBAT (Figure S11F and S11H). These results demonstrated that increased EE was not due to the metabolic alteration in distal tissues instead of the mitochondrial stress with the occurrence of ferroptosis in skeletal muscle.

Ferroptosis occurs in aged skeletal muscle

To analyse 2445 DEGs between aged and young mice and 1333 DEGs between *Tfr1*^{SC/WT} and *Tfr1*^{SC/KO} mice, 2203

common biomarkers were identified from two datasets. Among them, 72 genes were universally up-regulated, and 132 genes were down-regulated (Figure 7A and 7B). Through the KEGG pathway enrichment analysis for these common genes between two groups, ferroptosis, glutathione metabolism, and fatty acid biosynthesis were top candidate pathways, suggesting that skeletal muscle ageing may be accompanied by ferroptosis. Ferrozine assay to assess the serum and TA muscle NHI showed that compared with the young mice, aged mice had significantly higher iron levels (Figure 7D). Aged TA muscle expressed lower Tfr1, Nrf2, Gpx4, and Fth1 but higher Slc39a14, which mimics the gene expression pattern in *Tfr1*^{SC/KO} mice (TA muscle total protein, Figure 7E). Most importantly, TA muscle membrane Tfr1 protein was decreased to undetectable levels but with significantly higher expression levels of Slc39a14 (Figure 7E). These observations in together with previous observation in liver indicated that Slc39a14 may facilitate NTBI absorption in aged skeletal muscle causing iron accumulation in TA muscle to activate ferroptosis. Meanwhile, Ferro-1, as a ferroptosis inhibitor, was intraperitoneally injected into aged mice upon intramuscular injection of CTX to induce injury and regeneration. Thirty days after injection indeed improved running capacity, such as running time and distance (Figure 7F).

The last question we asked was whether labile iron accumulation, lipid biosynthesis, and ferroptosis activation-related gene expression pattern could be recapitulated in human sarcopenia. To answer this question, muscle samples of young (age <30 years old) and old (age >60 years old) individuals were collected from patients who experienced fracture and under clinical treatment at The Third Affiliated Hospital of Sun Yat-Sen University. Skeletal muscle biopsy samples were collected and stored in hospital biobank of -80°C freezer previously. Dysregulation of iron metabolism-related (*Slc39a14*), adipogenesis-related (*Pparγ*, *Adiponectin*, *Fasn*, and *Cd36*), and ferroptosis-related genes (*Hmox1*, *Sat1*, and *Ptgs2*) was also observed in sarcopenia samples (Figure 7G–7I). All of these data demonstrated that ferroptosis is one of unrecognized cell death forms in aged skeletal muscle other than well-known cell death forms including apoptosis, autophagy, and necroptosis.

Discussion

Programmed cell death, such as apoptosis, autophagy, and necrosis, is stimulated by external factors in response to muscle injury. Dysregulation of these processes results in muscular dystrophy and sarcopenia. Here, in our regeneration defect model, we are surprised to identify a new form of cell death, which has not been reported elsewhere in skeletal muscle. The newly defined iron-dependent cell death, also named ferroptosis, is activated during muscle regeneration with *Tfr1* deletion in SCs. This event is coupled with labile

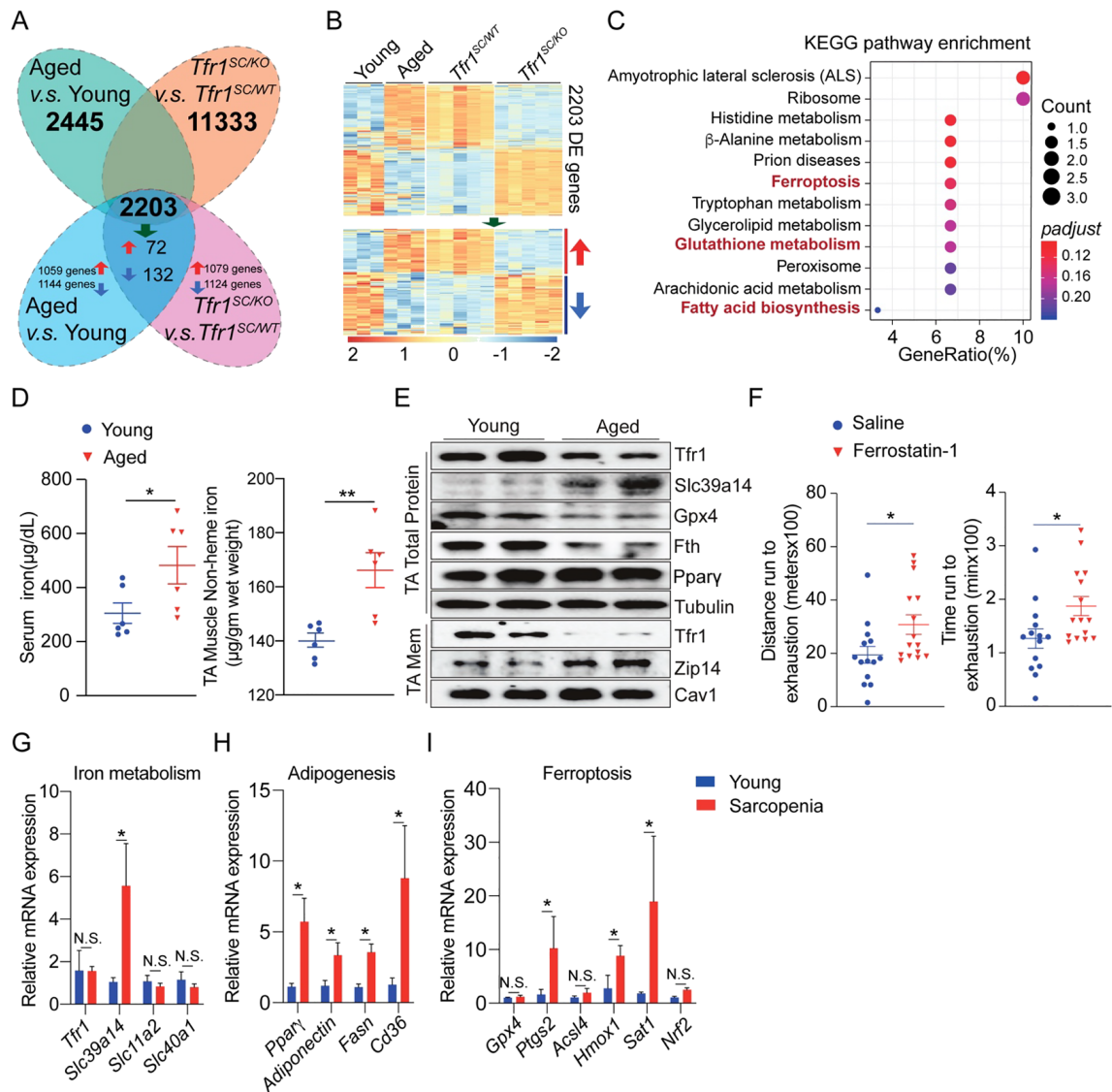


Figure 7 Slc39a14-mediated iron absorption and labile iron accumulation induces ferroptosis in aged skeletal muscle. (A) Venn diagram showing the overlapping genes between aged/young and *Tfr1^{SC/WT}/Tfr1^{SC/KO}* samples. (B) Heatmap of overlapping gene expression profile for aged/young group ($n = 3$) and *Tfr1^{SC/WT}/Tfr1^{SC/KO}* group ($n = 5$). (C) KEGG pathway enrichment analysis of up-regulated common genes identified ferroptosis-related genes highly expressed in transverse abdominal (TA) muscle of aged mice. (D) Serum and total TA muscle non-haem iron from young (8 weeks old) and aged (80 weeks old) *C57BL/6J* mice. (E) Representative western blot image of total and membrane protein of TA muscle from young (8 weeks old) and aged (80 weeks old) *C57BL/6J* mice. (F) Treadmill running distance and running time to exhaustion for aged (80 weeks old) *C57BL/6J* mice with cardiotoxin (CTX)-induced injury followed by intraperitoneal injection of either saline or ferrostatin-1 for 30 days ($n = 14$). qPCR analysis of iron metabolism-related (G), adipogenesis-related (H), and ferroptosis-related (I) gene expression in skeletal muscle biopsy sample from young and sarcopenia individuals. N.S., not significant, * $P < 0.05$, and ** $P < 0.01$, by two-sided Student's *t*-test. Data represent the mean \pm standard error of the mean.

iron accumulation, unsaturated fatty acid biosynthesis, and decreased expression of anti-ferroptosis biomarkers such as Gpx4 and Nrf2. Most importantly, the scenario of Tfr1–Slc39a14–iron axis is recapitulated in aged skeletal muscle of rodents and human sarcopenia, which provides physiological relevance of the Tfr1–Slc39a14–iron axis and ferroptosis in skeletal muscle, other than previously reported biological function of Slc39a14 in liver during iron overloading.^{16,17}

Iron homeostasis is indispensable to the proper function of skeletal muscle and postnatal regeneration, reflected from the importance of iron in mitochondrial respiration, ATP production, muscle contraction, and exercise capacity. This is partially due to the activity of the mitochondrial electron transport chain and mitochondrial clearance.¹⁸ These observations could be manipulated in murine models fed with iron-deprived diets, but muscular iron deficiency in patients

is usually accompanied by secondary diseases, such as congestive heart failure and chronic obstructive pulmonary disease.¹⁹ In terms of the developmental essentiality of iron, numerous studies have demonstrated that iron deficiency during pregnancy or the early stage of development causes growth retardation. However, a high systemic iron level is detrimental to the host, especially at advanced ages. Genome-wide association studies identified the association between healthy longevity and iron traits, for example, serum iron, transferrin level, and transferrin saturation.²⁰ Furthermore, individuals at advanced ages experience iron accumulation in multiple organs, such as brain, skeletal muscle, and liver.²¹ In contrast to iron deficiency, iron overloading or accumulation in tissues leads to increased oxidative stress by producing highly toxic hydroxyl radicals through the Fenton reaction. High iron content, especially the NHI, is associated with decreased muscle mass of both elderly human and aged rat.²² Evidences from different studies are consistent including ours that skeletal muscle of aged rodents has a phenotype of elevated NHI content, impaired muscle function, and muscular atrophy. In the *ex vivo* culture system, a high iron content decreases the myofibre survival rate, reduces SC cluster formation, and prohibits myoblast differentiation (Figure S4). However, the mechanisms causing iron accumulation and muscle loss remain unknown, which requires further exploration.

To delve into the pathogenic effect of iron and identify potential mediators, we utilized multiple approaches and models. As reported previously,²² we also noted declined *Tfr1* mRNA and protein in both skeletal muscles and SCs of aged mice but with higher NHI levels in skeletal muscle.²¹ We also found that the membrane Tfr1 protein is almost undetectable in aged mice (>80 weeks old) compared with young mice (~8 weeks old) (Figure 7E). To profile the expression of other iron absorption-related genes, *Slc11a2* and *Slc39a14* expression was up-regulated in TA muscle of 80-week-old mice (Figure 1D). However, *Slc11a2*-mediated TBI absorption in peripheral tissue relies on the membrane Tfr1 protein. Our work for the first-time identifies the phenomenon of Tfr1/*Slc39a14* expression switching in aged skeletal muscle. More specifically, *Slc39a14* expression is induced, and its protein is enriched on the cellular membrane to facilitate NTBI absorption to replace Tfr1 in aged individuals including rodents and human sarcopenia. This corresponds to our data of NHI accumulation in aged TA muscle. Our work provided evidence to interpret how labile iron is accumulated in the skeletal muscle of aged individuals.

Under physiological conditions, ferric iron in the form of TBI recognized by membrane Tfr1 is absorbed in peripheral tissues, such as adipose tissue.¹³ Multiple studies have shown that *Tfr1* deficiency results in functional disorder and even lethality. Mice with *Tfr1* conditional knockout in haematopoietic stem cells died within 1 week after birth.²³ Our previous study demonstrated that Tfr1 regulates

adipocyte thermogenesis and cell fate determination.¹³ Adipocytes with *Tfr1* ablation exhibit reduced thermogenic capacity and beigeing potential.¹³ Meanwhile, an alpha-skeletal actin (HSA)-driven Cre recombinase expression results in embryonic dysfunction of *Tfr1*, disrupting iron homeostasis and leading to the muscle growth retardation.¹⁰ This may be associated with dysfunction of haem-containing myoglobin synthesis and energy metabolism in muscle and liver.¹⁰ However, postnatal function of Tfr1 in skeletal muscle could not be well explored by utilizing this model as postnatal growth and regeneration of skeletal muscle rely on the activity of SCs. Thus, to solve this discrepancy, mice with conditional deletion of *Tfr1* in SCs were generated. In addition to regeneration defects, during muscle regeneration, we observed that failed SC activation and muscle regeneration, myoglobin degradation by haem oxygenase 1 (*Hmox1*), and up-regulation of *Slc39a14* expression may be three key factors contributing to labile iron accumulation, which may also be followed by decreased expression of *Fth1* and increased *de novo* unsaturated fatty acid biosynthesis. A similar observation was made in aged skeletal muscle of rodents and human sarcopenia: *Slc39a14* and *Hmox1* are up-regulated and the down-regulation of *Tfr1* and *Fth1* expression, which may contribute to the labile iron accumulation in skeletal muscle. A similar observation has been made in a model of macrophage-specific ferroportin (iron-exporting protein) ablation. In this model, monocyte-derived macrophages are indispensable in the damaged skeletal muscle to secrete pro-inflammatory or anti-inflammatory cytokines, which are necessary for the clearance of remnants and iron recycling. Although activated macrophages have a large portion of the intracellular labile iron pool, they have lower iron storage capacity and have to release iron into intracellular space to be utilized by newly formed myofibres.²⁴ Macrophage-mediated iron recycling and muscular regeneration must be well coordinated as macrophages only provide a temporary storage site for iron to prevent oxidative damage and then subsequently supply iron for muscle regeneration.

Well-coordinated iron recycling and utilization between macrophages and newly formed myofibres has been proven to be critical to muscular regeneration.²⁴ Thus, *Tfr1* ablation in SCs results in an excessive amount of iron released from macrophages to the labile iron pool in skeletal muscle, but is not to be absorbed because of the defect in functional myofibre formation, possibly due to irreversible depletion and cell-autonomous inactivation of SCs. Re-expression of Tfr1 protein *via* lentivirus infection partially decreases labile iron accumulation, prohibits fat biogenesis, and promotes regeneration. The labile iron accumulation for one aspect is derived from myoglobin degradation by *Hmox1*, and additional NTBI absorption is facilitated by *Slc39a14*, as the expression of both genes is up-regulated in *Tfr1*^{SC/KO} mice at 5 dpi and remains at higher expression levels at 9 and 15 dpi, which

definitely exacerbates iron accumulation and oxidative damage. It has been reported that in the absence of macrophage Fpn, iron sequestered inside the macrophages not only prevents muscle regeneration but also activates adipogenesis, leading to fat accumulation.²⁵ *Tfr1^{SC/KO}* mice present *de novo* lipogenesis instead of fatty acid uptake *via Cd36* by up-regulating expression of fatty acid synthase (*Fasn*) and activation of unsaturated fatty acid biogenesis pathway (e.g. *Scd1*, *Scd2*, *Fads1*, *Fads2*, and *Elvl5*). This is possible due to the activation of FAPs, a mesenchymal population located in the interstitial area of the skeletal muscle. FAPs are able to spontaneously differentiate into adipocyte or fibroblasts in *ex vivo* culture systems.²⁶ In *in vivo* system, FAPs are able to differentiate into adipocytes in degenerating dystrophic muscles while ectopic adipogenesis and fatty infiltration could be strongly inhibited by the presence of SC-derived myofibres.²⁷ Intramuscular fatty infiltration in skeletal muscle could be inhibited by IL-15 expression, possibly affecting FAP differentiation through Hedgehog signalling and other cytokines, for example, IL-4 and IL-13 secreted from eosinophils to remove cellular debris to enhance regeneration.²⁸ Skeletal muscle regeneration also requires network interactions among various cell types, such as endothelial cells, immune cells, and motor neurons.²⁹ Numerous studies have demonstrated that muscle regeneration begins from 3 to 5 days after injury and peaks on the second week after injury.³⁰ Single-cell sequencing data further demonstrate that skeletal muscle regeneration depends on a heterogeneous cell population and regulated by various intracellular and extracellular factors with the involvement of paracrine communication between SCs and non-myogenic cells at different regeneration stages.³¹ In *Tfr1^{SC/WT}* mice, we observed the peak of new myofibre formation at 5 dpi and almost complete of regeneration at 9 dpi as reported before,³¹ *Tfr1* ablation impairs cell-autonomous activation, proliferation, and differentiation, which significantly delays skeletal muscle regeneration. In the TA muscle of *Tfr1^{SC/KO}* mice, both *Pax7* and *MyoD* mRNAs were expressed at lower levels corresponding to decreased SC proliferation and less newly generated myofibres at 5 dpi. We also did not observe any changes in the expression of ferroptosis-related genes, such as *Gpx4* and *Ptgs2* at 5 dpi. However, as early as 5 dpi, some biomarkers that potentially contribute to the accumulation of labile iron, such as *Slc39a14* and *Hmox1*, were up-regulated in TA muscle of *Tfr1^{SC/KO}* mice, which could interpret the phenomenon of massive iron accumulation at later time points. Even though *MyoD* expression was up-regulated at 9 dpi (compared with *MyoD* expression at 5 dpi) in TA muscle of *Tfr1^{SC/KO}* mice, followed by the initiation of regeneration and a small number of eMyHC⁺ myofibres at small diameters, this may not have enough functional myofibres to utilize the iron and secrete cytokines to prevent adipogenesis from FAPs. Skeletal muscle regeneration is further exacerbated by down-regulation of *Gpx4*, an ROS scavenger, and *Fth1*, an important portion of

ferritin, as well as up-regulation of *Slc39a14*, an NTBI transporter and *Ptgs2*, involved in peroxidase generation at 9 dpi. The dysregulated iron homeostasis and adipogenesis result in activation of ferroptosis. Ferritin degradation via reduced *Fth1* expression is associated with activation of ferroptosis, which is defined as ferritinophagy.³² We believe that *Tfr1* ablation in SCs is a critical starting point of the skeletal muscle regeneration defects but not the ferroptosis marker, as reported before.³³ Most importantly, this *Tfr1* genetic deletion model and *Tfr1*–*Slc39a14* functional switching recapitulate a physiology-relevant down-regulation or dysfunction of *Tfr1* in skeletal muscle and SCs during ageing in skeletal muscle of rodents and human sarcopenia. Ferroptosis activation is orchestrated with decreased *Tfr1* membrane protein and *Slc39a14* membrane enrichment to facilitate NTBI iron absorption contributing to labile iron accumulation in aged skeletal muscle. Moreover, FAP-derived abnormal fibrosis and adipogenesis in aged muscle contributes to abnormal lipid and collagen accumulation,³⁴ together with iron accumulation and Fenton reaction leading to activation of ferroptosis in skeletal muscle.

In addition to ferroptosis-mediated dysregulation of iron and lipid metabolism in skeletal muscle, we have also observed systemic dysregulation of energy metabolism. Our electron transmission microscope data demonstrated that ferroptosis is followed by swollen mitochondria with irregular or disappeared cristae, immune cell infiltration, lysosome-mediated mitochondrial degradation or swollen mitochondria, and lipid droplets in a membrane surrounded structure with lysosome. Along with the ferroptosis in TA muscle of *Tfr1^{SC/KO}* mice, altered systemic energy metabolism is displayed with increased EE and expression of FGF21. FGF21 was initially discovered to be secreted from liver regulating energy balance and glucose and lipid metabolism.³⁵ In skeletal muscle under healthy and physiological conditions, its expression remains at a lower level. However, FGF21-induced muscle atrophy/weakness during fasting or FGF21 overexpression *in vivo* in muscle is sufficient to induce autophagy and muscle loss by 15%.³⁶ Its deletion could protect against muscle loss and weakness during fasting, which is accompanied by a significant reduction of mitophagy flux.³⁶ Other than its pathological function in skeletal muscle, FGF21 is a potent stimulator of adipocyte thermogenesis and nutrient metabolism to improve insulin sensitivity and reduce hepatic lipid accumulation.³⁷ Studies have suggested that autocrine and paracrine actions of FGF21 are able to induce thermogenesis with anti-obesity effects in adipocytes to improve glucose metabolism and lipid profiles.³⁸ For *Tfr1^{SC/KO}* mice, induction of FGF21 expression was accompanied by increased EE but not significant difference in the ratio of VCO_2/VO_2 . Thermogenic signalling pathway was also not observed, indicating that a *Ucp1*-independent mechanism may be involved. *Ucp1*-independent thermogenic pathways, such as creatine metabolism, calcium cycling, and amino acid

uncoupling, promote systemic energy metabolism.³⁹ FGF21 or FGF21 mimetic antibody stimulates brown or white adipocyte thermogenesis in a Ucp1-independent manner, which may act *via* directly promoting the host metabolic activity⁴⁰ or the FGFR1/bKlotho complex,⁴¹ respectively.

Meanwhile, resident and monocyte-derived macrophages also participate in the skeletal muscle regeneration at different stages. The depletion of macrophage in Tg-ITGAM-DTR mice impairs regeneration and results in the lipid accumulation in the skeletal muscle.⁴² Macrophages in skeletal muscle play a fundamental role in muscle repair and debris clearance. Upon initiation of muscle damage, infiltrated monocytes/neutrophils in injured areas differentiate into pro-inflammatory macrophage (M1 macrophage) with exposure to interferon- γ and tumour necrosis factor- α to phagocyte necrotic muscle debris.⁴³ M2 macrophage polarization majorly presents at the advanced stage of tissue repair and wound healing in concert with the secretion of IL-14 and IL13 from Th2 cytokines. Alternatively, M2 macrophages are also associated with the fibrosis in *mdx* mouse model, indicating that M2 macrophages may have alternative function under pathological condition.⁴⁴ Despite the compelling evidence of different macrophage subtypes during muscle repair, we identified a significant accumulation of M2 macrophages in the TA muscle of *Tfr1*^{SC/KO} mice, leading to the development of fibrosis and unexpected macrophage-derived foam cell differentiation. Foam cells are associated with the development of atherosclerosis and are also implicated in pro-inflammatory cytokine secretion, different inflammatory cells recruitment, and fibrotic collagen accumulation, which further exacerbates tissue function and impairs tissue repair.⁴⁵ However, the pathological function of foam cells in skeletal muscle requires further exploration.

In summary, our current investigation reveals that *Tfr1* deletion in SCs impairs skeletal muscle regeneration with activation of ferroptosis. This process is accompanied by functional switch of Tfr1–Slc39a14 to mediate NHI absorption and labile iron accumulation in the skeletal muscle. This phenomenon is recapitulated in the aged skeletal muscle, which shed light on the development of therapeutic strategies against muscular ageing and diseases.

Limitation of study

The present study has several limitations: first, the major focus of current investigation is Tfr1–iron axis during muscle ageing and regeneration. Whether Slc39a14 is a therapeutic target to ameliorate iron accumulation-induced muscle dysfunction requires further exploration. Second, we initially found that Tfr1 deletion in SCs followed by skeletal muscle regeneration results in regeneration impairment, labile iron accumulation, *de novo* PUFA biosynthesis, and glutathione metabolism disorder, leading to activation of ferroptosis.

As described in our manuscript, *Tfr1* depletion in SCs is an irreversible process, leading to a cell-autonomous defect of SC proliferation and differentiation. Thus, Ferro-1 is unable to rescue Tfr1 deletion-mediated ferroptosis. Moreover, Ferro-1 effectively improves aged skeletal muscle function, which may require further investigation to understand the molecular mechanism. Third, clinical relevance of Ferro-1 in improving muscle function in aged rodents and sarcopenia also needs in-depth exploration to pave road for clinical translation. Last, to understand the potential interaction between ferroptosis and other cell death (such as apoptosis, autophagy, and necrosis) at the molecular levels may require additional investigation for skeletal muscle of aged rodents, especially to integrate these pathways into the cellular events in order to pave the road to develop novel therapeutic strategies against muscular ageing and diseases.

Author contributions

Liwei Xie, Y.L., and X.Z. designed the experiment. H.D., S.C., X.Y., and X.D. developed and optimized the methodology. H.D., Z.L., X.M., Y.T., S.Z., B.L., G.C., Z.Y., X.Y., L.Y., X.C., J.S., H.C., Y.Y., G.X., H.L., W.W., Z.C., J.L., and J.H. collected and analysed the data. G.P., L.G., and M.H. raised the experimental mice. Liwei Xie acquired the grants and drafted the manuscript. We appreciated Mr Wei Zhao from Beijing Genomics Institute for assisting us the RNA sequencing and Ms Xiaochen Wang for the figure editing.

Acknowledgements

The authors of this manuscript certify that they comply with the ethical guidelines for authorship and publishing in the *Journal of Cachexia, Sarcopenia and Muscle*. We also appreciated Prof. Jun Hu from the Department of Orthopedics of The First Affiliated Hospital of Nanjing Medical University for providing a plenty of experimental resources during the Chinese New Year holiday for us to perform additional experiments to revise the manuscript and the valuable discussion. We appreciated Mr Wei Zhao from Beijing Genomics Institute for assisting us the RNA sequencing and Ms Xiaochen Wang for the figure editing.

Conflict of interest

None declared.

Funding

This work was supported by the National Basic Research Program of China (973 Program) (2017YFD0400301), Guangdong Academy of Sciences Project of Science and Technology Development (Grant Nos. 2016GDASRC-0202, 2018GDASXC-0102, and 2018GDASXC-0806), National Natural Science Foundation of China (Grant Nos. 81900797, 82072436, and 81672218) and Guangdong Basic and Applied Basic Research Foundation (Grant No. 2020B1515020046). In addition, Liwei Xie and Hongrong Ding are also the inventor for the patent of 2021101825711.

Data availability statement

RNA-Seq data are available upon request.

Online supplementary material

Additional supporting information may be found online in the Supporting Information section at the end of the article.

Figure S1. Related to Figure 1 Gene expression profile in four skeletal muscles (TA, EDL, Sol and Gas) across five different age stages (2wk-, 8wk-, 30wk-, 60wk- and 80wk-old). (A) Scheme of experimental design; (B) Heatmap of gene expression in TA from *C57BL/6J* mice across five different age-stage ($n = 3$ /group); (C) Heatmap of gene expression in EDL from *C57BL/6J* mice across five different age-stage ($n = 3$ /group); (D) Heatmap of gene expression in Sol from *C57BL/6J* mice across five different age-stage ($n = 3$ /group); (E) Heatmap of gene expression in Gas from *C57BL/6J* mice across five different age-stage ($n = 3$ /group).

Figure S2. Related to Figure 1 Gene expression profile in four skeletal muscles (TA, EDL, Sol and Gas) across five different age stages (2wk-, 8wk-, 30wk-, 60wk- and 80wk-old). (A) Heatmap of transition metal ion homeostasis related gene expression profile in TA muscle across five different age stages ($n = 3$ /group); (B) Heatmap of copper and zinc ion homeostasis related gene expression profile in TA muscle across five different age stages ($n = 3$ /group); (C) Total non-heme iron levels in four skeletal muscles between 2wk- and 8wk-old *C57BL/6J* mice ($n = 6$ /group); (D) qPCR analysis of *Tfr1* expression in TA muscle from *C57BL/6J* mice at 2wk-, 8wk-, 60wk-, and 80wk-old ($n = 6$ /group); (E) *Tfr1* protein expression level in TA muscle *C57BL/6J* mice at 2wk-, 8wk-, 60wk- and 80wk-old ($n = 6$ /group). N.S.: not significant, $**P < 0.01$, $***P < 0.005$, by 2-sided Student's t-test. Data represent the mean \pm SEM.

Figure S3. Related to Figure 1 *Tfr1* protein presents in proliferative SCs. (A) Representative images of myofibers from 8wk- and 80wk-old *C57BL/6J* mice ($n > 50$ myofibers from 5 mice/

group). Immunofluorescence of Pax7 (red), *Tfr1* (green), MyoD (pink) and DAPI (blue) staining revealed *Tfr1* protein is lowly expressed in SCs of old *C57BL/6J* mice; (B) Representative images of SCs cluster on single myofiber from adult *C57BL/6J* mice culture for different length of time (0, 24, 48 and 72-hr post single myofiber isolation); (C) Number of SC clusters, Pax7⁺ SCs per cluster, and Pax7⁺/MyoD⁻, Pax7⁺/MyoD⁺, and Pax7⁻/MyoD⁺ SCs per SCs cluster ($n > 50$ myofibers). N.S.: not significant, $**P < 0.01$, $***P < 0.005$, by 2-sided Student's t-test. Data represent the mean \pm SEM.

Figure S4. Related to Figure 1 Dysregulation of iron homeostasis inhibits SCs proliferation and differentiation. (A) Representative images of myofibers from adult *C57BL/6J* mice treated with DFO (an iron chelator) or vehicle ($n > 50$ myofibers from 5 mice/group). Immunofluorescence of Pax7 (red), *Tfr1* (green), MyoD (pink) and DAPI (blue) staining revealed iron deprivation inhibit SCs proliferation; (B) Number of SC clusters per myofiber; (C) Representative images of SCs differentiated into myotube with DFO treatment or vehicle. Immunofluorescence of Pax7 (red), MyoD (green), MHC (pink) and DAPI (blue) staining revealed iron deprivation inhibits SCs differentiation; (D) Summary of fusion index between control and DFO treatment group; (E) Overall survival rate of *ex vivo* cultured myofibers treated with different concentration of FAC (0, 5, 10, 25, 50, and 75 μ m). The number of survived myofiber was counted every 24-hr. (F) Number of SC clusters per myofiber treated with different concentration of FAC (0, 5, 10, 25, 50, and 75 μ m) and cultured for 72-hr; (G) Representative images of SCs differentiated into myotube with FAC treatment (25 μ m). Immunofluorescence of Pax7 (red), MyoD (green), MHC (pink) and DAPI (blue) staining revealed FAC treatment at higher concentration inhibits SCs differentiation; (H) Fusion index of SCs differentiation with FAC treatment. N.S.: not significant, $***P < 0.005$, by 2-sided Student's t-test. Data represent the mean \pm SEM.

Figure S5. Related to Figure 2 *Tfr1*-ablation in myoblasts prevents the proliferation. Pax7⁺ SCs were isolated from *Tfr1^{fl/fl}* mice and culture with F10 medium. Myoblasts were treated with Adenovirus expression Cre recombinase or GFP as control. 24-hr later, myoblasts were further treated with EdU for 24-hr before immunostaining. (A) Representative images of myoblasts immunostaining with EdU (green), *Tfr1* (red) and DAPI (blue) indicates that *Tfr1*-ablation inhibits myoblast proliferation; (B) Number of EdU⁻ and EdU⁺ myoblasts in total DAPI⁺ myoblast from both control and *Tfr1*-deleted group; (C) Representative images of myoblasts immunostaining with EdU (red) and DAPI (blue) indicates that *Tfr1*-ablation inhibits myoblast proliferation; (D) Stacking bar graph showing the ratio of EdU⁻ and EdU⁺ myoblasts. N.S.: not significant, $***P < 0.005$, by 2-sided Student's t-test. Data represent the mean \pm SEM.

Figure S6. Related to Figure 2 *Tfr1*-knockdown in C2C12 myoblasts prevents the differentiation. (A) Schematic cartoon depicting the experimental design of C2C12 with

Tfr1 knockdown by gRNAs; (B) *Tfr1* protein level in C2C12 myoblasts with *Tfr1* knockdown by gRNAs under condition of growth medium (GM) or differentiation medium (DM); (C) Representative images of *Tfr1* (green) and MHC (purple) immunostaining in 7 days differentiated C2C12 myoblasts with *Tfr1* knockdown by gRNAs; (D) Fusion index of differentiated C2C12 myoblasts with *Tfr1* knockdown by gRNAs; (E) Scheme of experimental design of C2C12 myoblasts with *Tfr1* siRNA transient transfection; (F) qRT-PCR analysis of *Tfr1* expression in C2C12 myoblasts with transient transfection of *Tfr1* siRNA; (G) Representative image of western blot of *Tfr1* protein expression in C2C12 myoblasts with transient transfection of *Tfr1* siRNAs; (H) Representative images of *Tfr1* (green) and MHC (purple) immunostaining in 3 days differentiated C2C12 myoblasts with transient transfection of *Tfr1* siRNAs; (I) Fusion index of differentiated C2C12 myoblasts with transient transfection of *Tfr1* siRNAs. $^{**}P < 0.01$, $^{***}P < 0.005$, by 2-sided Student's t-test. Data represent the mean \pm SEM.

Figure S7. Related to Figure 3 *Tfr1*-ablation in SCs inhibits SCs proliferation and skeletal muscle regeneration. (A) qPCR analysis of *Tfr1*, *Pax7* and *MyoD* expression in TA muscle from *Tfr1^{SC/WT}* and *Tfr1^{SC/KO}* mice after CTX-induced injury at 5 and 9 dpi; (B) qPCR analysis of *Tfr1*, *Pax7* and *MyoD* expression in TA muscle of *Tfr1^{SC/WT}* and *Tfr1^{SC/KO}* mice after CTX-induced injury at 30 dpi; (C) Representative images of TA section H.E. staining of *Tfr1^{SC/WT}* and *Tfr1^{SC/KO}* mice after CTX-induced injury at 5 and 9 dpi; (D) Representative images of TA section Masson staining of *Tfr1^{SC/WT}* and *Tfr1^{SC/KO}* mice after CTX-induced injury at 5 and 9 dpi; (E) Summary of collagen volume fraction on TA section of *Tfr1^{SC/WT}* and *Tfr1^{SC/KO}* mice after CTX-induced injury at 5 and 9 dpi. N.S.: not significant, $^{***}P < 0.005$, by 2-sided Student's t-test. Data represent the mean \pm SEM.

Figure S8. Related to Figure 4 Gene expression profile in TA muscle between *Tfr1^{SC/WT}* and *Tfr1^{SC/KO}* mice after CTX-induced injury at 30 dpi. (A) Timeline for tamoxifen-induced *Tfr1* deletion and CTX-induced TA muscle injury; (B) Heatmap of macrophage-derived foam cell differentiation related gene expression; (C) Heatmap of collagen biosynthetic process related gene expression; (D) Heatmap of lipid biosynthetic process related gene expression; (E) Heatmap of macrophage activation related gene expression; (F) Heatmap of fatty acid β -oxidation related gene

expression; (G) Heatmap of muscle cell differentiation related gene expression; (H) Heatmap of tricarboxylic acid cycle related gene expression; (I) Heatmap of mitochondrial respiratory chain complex assembly related gene expression.

Figure S9. Related to Figure 5 TA of *Tfr1^{SC/KO}* mice has different metabolic profiling. (A) GSH level in TA muscle of *Tfr1^{SC/WT}* and *Tfr1^{SC/KO}* mice after CTX-induced injury ($n = 5$ /group); (B) GSSG level in TA muscle of *Tfr1^{SC/WT}* and *Tfr1^{SC/KO}* mice after CTX-induced injury ($n = 5$ /group); (C) Ratio of GSH/GSSG in TA muscle of *Tfr1^{SC/WT}* and *Tfr1^{SC/KO}* mice after CTX-induced injury ($n = 5$ /group); (D) MDA level in TA muscle of *Tfr1^{SC/WT}* and *Tfr1^{SC/KO}* mice after CTX-induced injury at 30 dpi ($n = 5-7$ /group); (E) Heatmap presenting the amount of SFAs, MUFAs and PUFA between *Tfr1^{SC/WT}* and *Tfr1^{SC/KO}* mice after CTX-induced injury; (F) PCA of lipid profiling between *Tfr1^{SC/WT}* and *Tfr1^{SC/KO}* mice after CTX-induced injury; (G) Bar graph showing the predicted pathway enrichment.

Figure S10. Related to Figure 6 *Slc39a14*-mediated NTBI absorption exacerbates skeletal muscle ferroptosis for *Tfr1^{SC/KO}* mice. (A) Ratio of TA/body weight between *Tfr1^{SC/WT}* and *Tfr1^{SC/KO}* mice after CTX-induced injury at 5, 9 and 15 dpi; (B-G) qPCR analysis of *Slc11a2*, *Slc39a14*, *Fth1*, *Ftl*, *Hmox1*, *Slc3a2* expression in TA muscle of *Tfr1^{SC/WT}* and *Tfr1^{SC/KO}* mice after CTX-induced injury at 5, 9 and 15 dpi; (H) Representative western blot images of protein level in TA between *Tfr1^{SC/WT}* and *Tfr1^{SC/KO}* mice after CTX-induced injury at 30 dpi; (I) Ratio of tissue (TA, iBAT and iWAT)/body weight between *Tfr1^{SC/WT}* and *Tfr1^{SC/KO}* mice after CTX-induced injury at 30 dpi. N.S.: not significant, $^{*}P < 0.05$, $^{**}P < 0.01$, $^{***}P < 0.005$, by 2-sided Student's t-test. Data represent the mean \pm SEM.

Figure S11. Related to Figure 6 SC-specific *Tfr1* deletion induced TA muscle regeneration defect does not perturb systemic metabolism. (A, C, E and G) qPCR analysis of iron metabolism and thermogenesis related gene expression in Liver (A), iBAT (C), iWAT (E) and eWAT (G) between *Tfr1^{SC/WT}* and *Tfr1^{SC/KO}* mice after CTX-induced injury at 30 dpi. (B, D, F and H) Representative western blot images of protein level in Liver (B), iBAT (D), iWAT (F) and eWAT (I) between *Tfr1^{SC/WT}* and *Tfr1^{SC/KO}* mice after CTX-induced injury at 30 dpi. N.S.: not significant, $^{**}P < 0.01$, $^{***}P < 0.005$, by 2-sided Student's t-test. Data represent the mean \pm SEM ($n = 6$ /group).

References

- Raff M. Cell suicide for beginners. *Nature* 1998;**396**:119–122.
- Sciorati C, Rigamonti E, Manfredi AA, Rovere-Querini P. Cell death, clearance and immunity in the skeletal muscle. *Cell Death Differ* 2016;**23**:927–937.
- Tsujimoto Y. Multiple ways to die: non-apoptotic forms of cell death. *Acta Oncol* 2012;**51**:293–300.
- Dixon SJ, Lemberg KM, Lamprecht MR, Skouta R, Zaitsev EM, Gleason CE, et al. Ferroptosis: an iron-dependent form of nonapoptotic cell death. *Cell* 2012;**149**:1060–1072.
- Fang X, Wang H, Han D, Xie E, Yang X, Wei J, et al. Ferroptosis as a target for protection against cardiomyopathy. *Proc Natl Acad Sci U S A* 2019;**116**:2672–2680.

6. Yu Y, Jiang L, Wang H, Shen Z, Cheng Q, Zhang P, et al. Hepatic transferrin plays a role in systemic iron homeostasis and liver ferroptosis. *Blood* 2020;**136**:726–739.
7. Yin H, Price F, Rudnicki MA. Satellite cells and the muscle stem cell niche. *Physiol Rev* 2013;**93**:23–67.
8. Chen F, Zhou J, Li Y, Zhao Y, Yuan J, Cao Y, et al. YY 1 regulates skeletal muscle regeneration through controlling metabolic reprogramming of satellite cells. *EMBO J* 2019;**38**:1–23.
9. Xie L, Yin A, Nichenko AS, Beedle AM, Call JA, Yin H. Transient HIF2A inhibition promotes satellite cell proliferation and muscle regeneration. *J Clin Invest* 2018;**128**:2339–2355.
10. Barrientos T, Laothamatas I, Koves TR, Soderblom EJ, Bryan M, Moseley MA, et al. Metabolic catastrophe in mice lacking transferrin receptor in muscle. *EBioMedicine* 2015;**2**:1705–1717.
11. Li Y, Cheng JX, Yang HH, Chen LP, Liu FJ, Wu Y, et al. Transferrin receptor 1 plays an important role in muscle development and denervation-induced muscular atrophy. *Neural Regen Res* 2021;**16**:1308–1316.
12. Altun M, Edström E, Spooner E, Flores-Morales A, Bergman E, Tollet-Egnell P, et al. Iron load and redox stress in skeletal muscle of aged rats. *Muscle Nerve* 2007;**36**:223–233.
13. Li J, Pan X, Pan G, Song Z, He Y, Zhang S, et al. Transferrin receptor 1 regulates thermogenic capacity and cell fate in brown/beige adipocytes. *Adv Sci* 2020;**7**.
14. Chen S, Ding H, Yao X, Xie L. Isolation and culture of single myofiber and immunostaining of satellite cells from adult C57BL/6J mice. *Bio-pro* 2019;**9**:e3313.
15. Forsström S, Jackson CB, Carroll CJ, Kuronen M, Pirinen E, Pradhan S, et al. Fibroblast growth factor 21 drives dynamics of local and systemic stress responses in mitochondrial myopathy with mtDNA deletions. *Cell Metab* 2019;**30**:1040–1054.e7.
16. Juan PL, Fikret A, Hyeyoung N, et al. Zip14 (Slc39a14) mediates non-transferrin-bound iron uptake into cells. *Proc Natl Acad Sci U S A* 2006;**14**:10–15.
17. Jenkitkasemwong S, Wang CY, Coffey R, Zhang W, Chan A, Biel T, et al. SLC39A14 is required for the development of hepatocellular iron overload in murine models of hereditary hemochromatosis. *Cell Metab* 2015;**22**:138–150.
18. Leermakers PA, Remels AHV, Zonneveld MI, Rouschop KMA, Schols AMWJ, Gosker HR. Iron deficiency-induced loss of skeletal muscle mitochondrial proteins and respiratory capacity; the role of mitophagy and secretion of mitochondria-containing vesicles. *FASEB J* 2020;**34**:6703–6717.
19. Tkaczyszyn M, Drozd M, Węgrzynowska-Teodorczyk K, Flinta I, Kobak K, Banasiak W, et al. Depleted iron stores are associated with inspiratory muscle weakness independently of skeletal muscle mass in men with systolic chronic heart failure. *J Cachexia Sarcopenia Muscle* 2018;**9**:547–556.
20. Wilson JF, Joshi PK. Multivariate genomic scan implicates novel loci and haem metabolism in human ageing. *Nat Commun* 2020;**1**–10.
21. Xu J, Knutson MD, Carter CS, Leeuwenburgh C. Iron accumulation with age, oxidative stress and functional decline. *PLoS One* 2008;**3**:e2865.
22. DeRuisseau KC, Park Y-M, DeRuisseau LR, Cowley PM, Fazen CH, Doyle RP. Aging-related changes in the iron status of skeletal muscle. *Exp Gerontol* 2013;**48**:1294–1302.
23. Wang S, He X, Wu Q, Jiang L, Chen L, Yu Y, et al. Transferrin receptor 1-mediated iron uptake plays an essential role in hematopoiesis. *Haematologica* 2020;**105**:2071–2082.
24. Gaetano C, Massimo L, Alberto M. Control of iron homeostasis as a key component of macrophage polarization. *Haematologica* 2010;**95**:1801–1803.
25. Corna G, Caserta I, Monno A, Apostoli P, Manfredi AA, Camaschella C, et al. The repair of skeletal muscle requires iron recycling through macrophage ferroportin. *J Immunol* 2016;**197**:1914–1925.
26. Marinkovic M, Fuoco C, Sacco F, Cerquone Perpetuini A, Giuliani G, Micarelli E, et al. Fibro-adipogenic progenitors of dystrophic mice are insensitive to NOTCH regulation of adipogenesis. *Life Sci Alliance* 2019;**2**:e201900437.
27. Uezumi A, Fukada SI, Yamamoto N, Takeda S, Tsuchida K. Mesenchymal progenitors distinct from satellite cells contribute to ectopic fat cell formation in skeletal muscle. *Nat Cell Biol* 2010;**12**:143–152.
28. Kopinke D, Roberson EC, Reiter JF. Ciliary Hedgehog signaling restricts injury-induced adipogenesis. *Cell* 2017;**170**:340–351.e12.
29. Biferali B, Proietti D, Mozzetta C, Madaro L. Fibro-adipogenic progenitors cross-talk in skeletal muscle: the social network. *Front Physiol* 2019;**10**:1–10.
30. Huard J, Li Y, Fu FH. Muscle injuries and repair: current trends in research. *J Bone Joint Surg Am* 2002;**84**:822–832.
31. Oprescu SN, Yue F, Qiu J, Brito LF, Kuang S. Temporal dynamics and heterogeneity of cell populations during skeletal muscle regeneration. *iScience* 2020;**23**:100993.
32. Gao M, Monian P, Pan Q, Zhang W, Xiang J, Jiang X. Ferroptosis is an autophagic cell death process. *Cell Res* 2016;**26**:1021–1032.
33. Feng H, Schorpp K, Jin J, Yozwiak CE, Hoffstrom BG, Decker AM, et al. Transferrin receptor is a specific ferroptosis marker. *Cell Rep* 2020;**30**:3411–3423.e7.
34. Joe AWB, Yi L, Natarajan A, Le Grand F, So L, Wang J, et al. Muscle injury activates resident fibro/adipogenic progenitors that facilitate myogenesis. *Nat Cell Biol* 2010;**12**:153–163.
35. Owen BM, Mangelsdorf DJ, Kliewer SA. Tissue-specific actions of the metabolic hormones FGF15/19 and FGF21. *Trends Endocrinol Metab* 2015;**26**:22–29.
36. Oost LJ, Kustermann M, Armani A, Blaauw B, Romanello V. Fibroblast growth factor 21 controls mitophagy and muscle mass. *J Cachexia Sarcopenia Muscle* 2019;**10**:630–642.
37. Kharitonov A, DiMarchi R. FGF21 revolutions: recent advances illuminating FGF21 biology and medicinal properties. *Trends Endocrinol Metab* 2015;**26**:608–617.
38. Badman MK, Pissios P, Kennedy AR, Koukos G, Flier JS, Maratos-Flier E. Hepatic fibroblast growth factor 21 is regulated by PPAR α and is a key mediator of hepatic lipid metabolism in ketotic states. *Cell Metab* 2007;**5**:426–437.
39. Kazak L, Chouchani ET, Jedrychowski MP, Gygi SP, Bruce M, Kazak L, et al. A creatine-driven substrate cycle enhances energy expenditure and thermogenesis in beige fat. *Cell* 2015;**163**:643–655.
40. Keipert S, Lutter D, Schroeder BO, Brandt D, Stählmann M, Schwarzmayr T, et al. Endogenous FGF21-signaling controls paradoxical obesity resistance of UCP1-deficient mice. *Nat Commun* 2020;<https://doi.org/10.1038/s41467-019-14069-2>
41. Chen MZ, Chang JC, Zavala-solorio J, Kates L, Thai M, Ogasawara A, et al. FGF21 mimetic antibody stimulates UCP1-independent brown fat thermogenesis via FGFR1/b Klotho complex in non-adipocytes. *Mol Metab* 2017;**6**:1454–1467.
42. Id LM, Id AT, de Bardi M, Id FFC, Id MP, Id GRD, et al. Macrophages fine tune satellite cell fate in dystrophic skeletal muscle of mdx mice. *PLoS Biol* 2019;**1**–29.
43. Mantovani A, Sica A, Sozzani S, Allavena P, Vecchi A, Locati M. The chemokine system in diverse forms of macrophage activation and polarization. *Trends Immunol* 2004;**25**:677–686.
44. Villalta SA, Nguyen HX, Deng B, Gotoh T, Tidball JG. Shifts in macrophage phenotypes and macrophage competition for arginine metabolism affect the severity of muscle pathology in muscular dystrophy. *Hum Mol Genet* 2009;**18**:482–496.
45. Thomas AC, Eijgelaar WJ, Daemen MJAP, Newby AC. The pro-fibrotic and anti-inflammatory foam cell macrophage paradox. *Genomics data* 2015;**6**:136–138.